UNIVERSITY OF PÉCS

Doctoral School of Physics

Laser physics, nonlinear optics, and spectroscopy Program

Determination of multiphoton absorption coefficients in lithium niobate and lithium tantalate crystals by the Z-scan technique

Ph.D. Thesis

Imene Benabdelghani

Supervisor:

Dr. Gyula Polónyi

Pécs 2024

Acknowledgments

This thesis represents the results of research performed at the high-field terahertz (THz) laboratory from the Institute of Physics at Szentágothai Research Centre and the Ultrafast, High-intensity Light-matter Interactions Laboratory from the Institute for Solid State Physics and Optics at the Wigner Research Centre. I am grateful for all the experience I gained, thanks in large part to the following individuals for giving me the strength and perseverance to come out in the end with my thesis completed. I am deeply grateful to Prof. Dr. János Hebling for accepting me as a Ph.D. student. He allowed me the opportunity to pursue the work in this thesis which I otherwise may not have gotten. I am very appreciative of his help and guidance, who provided the topic of this thesis. He also generously offered his lab resources, materials, and his vast reservoir of knowledge, which have been instrumental in shaping my research. I extend my heartfelt appreciation to him for introducing me to the field of nonlinear optics, a subject I had little familiarity with before joining his research group. His patient guidance and insightful teachings have been significant in my development.

I have no words to pay my thanks to my supervisor Dr. Gyula Polónyi. He was a continuous source of inspiration during my PhD studies. He was always helpful and supportive of me, and I found him accommodating and knowledgeable. He always pushed me to work and gave me the full independence to work. He motivated me to pursue my research on this topic and I learned a lot from him on my research topic. He provided me good, comfortable, and supportive research environment. He is a compassionate and kind-hearted person.

I would like to express my appreciation to Dr. Gábor Bazsó, for the great help in this work his professional suggestions have inspired me and provided great assistance towards this work. I am particularly grateful to him for being patient with me when we spent numerous hours in the laboratory to obtain accurate and reliable results. His nice and encouraging attitude was a blessing for me.

My sincere thanks go to Dr. György Tóth for his generous collaboration substantially extended the scope of this thesis. I am grateful for the code he provided that I used to evaluate the obtained results in this thesis, and for the hours he spent helping me.

I would also like to thank all my colleagues at the Szentágothai THz laboratory who have provided invaluable help and exchanged fructiferous views from time to time that have been vital to my progress. I am grateful to all the staff members of the Institute of Physics at the University of Pécs for their encouragement and support during my study.

I would like to thank my parents, for all their love, patience, understanding, and extensive support throughout these years, and for being a sounding board for me reflecting upon all my decisions.

Lastly, I am profoundly grateful to the Stipendium Hungaricum Scholarship program for generously funding my doctoral study, which has opened up countless opportunities for personal and academic growth.

For all I mentioned above …all appreciation and respect

Abstract

In recent years, there has been a notable interest in multi-photon absorption mechanisms. This growing interest is due to their useful applications in several research fields such as optical limiting, data storage, and biomedical research. One of the most extensively researched processes to date is two-photon absorption (2PA). In the past two decades optical rectification of femtosecond near-infrared pulses in lithium niobate (LN, $LiNbO_3$) has become the most widespread way to generate high energy terahertz (THz) pulses in the low part of the THz spectrum (0.1 – 2 THz). Besides LN, lithium tantalate (LT, $LiTaO_3$), another ferroelectric crystal from the same symmetry class, is also a material of interest in terms of THz generation. Recently, substantial effort has been made to overcome the limitations of the conventional tilted-pulse-front pumped setup and more detailed theoretical models have been created to compare the performances of the newly suggested setups, despite one of the main limitation factors on the maximum usable pump intensity being the free-carrier absorption in the THz range induced by multiphoton absorption of the pump. To overcome these limitations, open-aperture Z-scan measurements have been carried out to investigate the three-photon (3PA) in LN and LT, and four-photon absorption (4PA) in LN congruent (cLN, cLT) and stoichiometric (sLN, sLT) crystals at 800 nm and 1030 nm wavelengths, respectively for different Mg doping concentrations. The laser pulse duration at the two wavelengths was 40 and 190 fs, respectively. Both ordinary and extraordinary polarization were considered. The peak intensity inside the crystals varied between approximately 110 and 555 GW/cm^2. The 3PA and 4PA coefficients were evaluated using a theoretical model. In the case of LN crystals, the results suggest that their minima are at or around the Mg doping level corresponding to the threshold for suppressing photo-refraction for both cLN and sLN. This result can be attributed to the contribution of crystal defects to the 3PA and 4PA processes. Furthermore, the 4PA at 1030 nm exhibited greater nonlinear absorption than the 3PA at 800 nm under the same intensity level. Possible reasons for this unexpected behaviour are discussed. In the case of LT crystals, the outcomes reveal that the dominant multi-photon absorption with this pumping wavelength is three-photon absorption (3PA) and a decline of the 3PA coefficient is demonstrated with increasing pumping intensity. Surprisingly, larger 3PA coefficients were measured for LT than for LN, contrary to the larger bandgap of LT in comparison to LN. Overall, comparing the 3PA and 4PA values of these crystals will enable for selection of the optimum composition of LN and LT crystals for efficient THz generation and other nonlinear optical processes requiring high pump intensities.

Table of Contents

Contents

Acknowledgments....ii
Abstract....iii
Table of Contents....iv
List of Figures....vi
List of Abbreviations....ix
List of Symbols....x
Chapter One: Introduction....1
1.1 Background and Motivation....1
1.2 Dissertation Outline....3
Chapter Two: Properties of the Examined Materials....5
2.1 Lithium niobate....5
2.2 Lithium tantalate....7
Chapter Three: Nonlinear Optical Properties....9
3.1 Multi-photon absorption....10
3.2 Free carrier absorption....12
3.3 Other interaction between light and matter and related phenomena....13
3.3.1 Second harmonic generation....13
3.3.2 Coherence length....14
Chapter Four: Z-scan Technique....16
4.1 Tool for method: Gaussian beam, Knife edge method....16
4.1.1 Gaussian beam....16
4.1.2 Knife-edge method....20
4.2 Interpretation of Z-scan....22
4.2.1 Open-aperture....23
4.3 Determining nonlinear refractive index and absorption coefficients....23
4.4 Evaluation of multiphoton absorption coefficients....26
4.4.1 Numerical model....26
Chapter Five: Motivation of the work and objectives....29
Chapter Six: Materials and Methods....31
6.1 Experimental setups....31
6.1.1 Z-scan setup for 800 nm laser....31
6.1.2 Z-scan setup for 1030 nm laser....32

6.2 Beam radius measurements 33
6.2 Sample preparation 35
6.4 UV absorption spectra 36
Chapter Seven: Results 39
7.1 Z-scan curves obtained for 800 nm laser 39
7.1.1 Lithium niobate 39
7.1.2 Lithium tantalate 42
7.2 Z-scan curves obtained for 1030 nm laser 46
7.2.1 Lithium niobate 46
Chapter Eight: Discussion 49
8.1. Multiphoton absorption in LN 49
8.2. Multiphoton absorption in LT 53
8.3. Comparison 55
Chapter Nine: Conclusion 57
9.1 Conclusion 57
Chapter Ten: Thesis Statements 58
10.1 Thesis statements 58
Chapter Eleven: Hungarian summary 60
11.1 Összefoglaló 60
11.1.1 Absztrakt 60
11.1.2 Tézispontok 61
Chapter Twelve: English summary 64
12.1 Summary 64
12.1.1 Introduction 64
12.1.2 Objectives and methods 65
12.1.3 New scientific results 66
References 71
Funding 76

List of Figures

Figure 2-1: Crystal structure of $LiNbO_3$ [49] 6

Figure 2-2: Crystal structure of $LiTaO_3$ [26,76]. 8

Figure 3-1: (a) Geometry of SHG. (b) Energy-level diagram describing SHG [83]. 13

Figure 3-2: Vector diagrams for the SHG process for (a) co- and (b) counter-propagating beams [84]. 13

Figure 4-1: Gaussian beam parameters associated with beam waist(w_0), Rayleigh length (z_R) and angular divergence [89]. 17

Figure 4-2: Principle of the knife edge measurement. b): The typical curve obtained during the measurement by the Knife Edge method [98]. 21

Figure 4-3: A schematic setup of closed aperture (a) and open aperture (b) Z-scan technique. L_f: focusing lens, L_c: collecting lend, NDF: neutral density filter, PD: photodiode [19] 22

Figure 6-1: Schematic of the z-scan experimental setup. HWP: half-wave plate, LP: linear polarizer, PD: photodiode, ND10A: neutral density filter, +z shows the positive direction toward the detector, -z shows the negative direction toward the focusing lens [121] 32

Figure 6-2: Schematic of the z-scan experimental setup. HWP: half-wave plate, TFP: thin film polarizer, PD: photodiode, +z shows the positive direction toward the detector, -z shows the negative direction toward the focusing lens [115] 32

Figure 6-3: The measured horizontal and vertical spot sizes versus the propagation coordinate for 0.8 μm (a) and 1.03 μm (b). The same indicated for an about $\pm 3z/z_R$ range (c,d). Relative intensity curves calculated with the original and the shifted data (e,f) [115] 34

Figure 6-4: UV absorption spectra for all the investigated crystals in lithium niobate for both ordinary and extraordinary polarized light [115] 37

Figure 6-5: UV absorption spectra for all the investigated crystals in lithium tantalate for both ordinary and extraordinary polarized light [121]. 38

Figure 6-6: As an example, the directly measured z-scan curve (a), measured with 1.03 μm beam and the symmetrized curve (b) is shown in the case of sLN:1.50% Mg crystal for ordinary polarization [115]. 38

Figure 7-1: Result of z-scan measurements (dots) together with fitting curves for different crystals and laser intensities. The 3PA coefficients resulting the best fitting are indicated. β_3 is measured in cm^3/GW^2 [115] 40

Figure 7-2: Result of the z-scan measurements (dots) together with fitting curves for sLN (a) and cLN (b) at 290 GW/cm^2 for different crystal compositions. β_3 is measured in cm^3/GW^2 [115] 41

Figure 7-3: Normalized 3PA coefficients versus different Mg doping concentrations at different pump intensities 42

Figure 7-4: As an example, the result of the z-scan measurements (dots) together with fitting curves of 3PA (red line) and 4PA (blue line) for sLT:0.5% Mg crystal, ordinary (a) and extraordinary (b) polarization at 360 GW/cm^2 [121]. 43

Figure 7-5: Result of z-scan measurements (dots) together with fitting curves for different LT crystals at different laser intensities. The 3PA coefficients resulting the best fitting are indicated in cm^3/GW^2 [121]. 45

Figure 7-6: Result of the z-scan measurements (dots) together with fitting curves for cLN (a, c) and sLN (b, d) crystals with different Mg doping levels at 180 GW/cm^2 laser intensity for extraordinary (a,b) and ordinary (c,d) polarization. β_4 is measured in cm^5/GW^3 [115]. 48

Figure 8-1: Three-photon absorption coefficients of cLT and sLT crystals versus the pumping intensities for ordinary (a) and extraordinary (b) polarization [121]. 53

Figure 8-2: Fitting for saturation intensity to the obtained coefficients. I_{sat} in the legend corresponds to the saturation intensity [121]. 54

List of Tables

Table 6-1: Beam parameters of the 0.8 μm beam determined by the knife-edge method 35

Table 6-2: Beam parameters of the 1.03 μm beam determined by the knife-edge method 35

Table 6-3: Parameters of the studied samples.....36

Table 7-1: Three-photon absorption coefficients of all LN samples for extraordinary polarization 41

Table 7-2: Three-photon absorption coefficients in Lithium tantalate for ordinary and extraordinary polarization.....46

Table 7-3: Four-photon effective absorption coefficients of all samples for ordinary and extraordinary polarization.....48

Table 8-1: Calculated coherence length (l_c) for second harmonic generation (SHG) in both oo-e and ee-e SHG processes in a few LN crystal compositions. n_o and n_e are the refractive indices for ordinary and extraordinary polarizations, respectively 52

Table 8-2: Calculated coherence length (l_c) for second harmonic generation (SHG) in both oo-e and ee-e SHG processes in LT crystals. no and ne are the refractive indices for ordinary and extraordinary polarizations, respectively.....55

Table 8-3: Comparison of the calculated 3PA coefficients of LN and LT for extraordinary polarization at 800 nm wavelength for 255 GW/cm^2 and 240 GW/cm^2 intensity, respectively 56

List of Abbreviations

BS Beam Splitter

OR Optical rectification

SHG Second Harmonic Generation

THG Third Harmonic Generation

FCA Free Carrier Absorption

MPA Multiphoton Absorption

ODT Optical Damage Thresholds

sLN/cLN stoichiometric/congruent lithium niobate

sLT/cLT stoichiometric/congruent lithium tantalate

PFT Pulse Front Tilt

FWHM Full Width at Half Maximum

2PA Two-photon absorption

3PA Three-photon absorption

4PA Four-photon absorption

List of Symbols

α	Linear absorption coefficient
τ	Pulse duration
c	Speed of light in vacuum
P	Polarization
ϵ_o	Permittivity of free space
I	Intensity
E	Electric field
$\chi^{(1)}$	Linear susceptibility
$\chi^{(2)}$	Second order nonlinear susceptibility
$\chi^{(3)}$	Third-order nonlinear susceptibility
L	crystal length
E_g	Bandgap energy
l_c	Coherence length

Chapter One: Introduction

1.1 Background and Motivation

Terahertz (THz) radiation falls within the electromagnetic spectrum, positioned between microwaves and infrared radiation. The range spans approximately from 0.1 to 10 THz on the electromagnetic spectrum. From the mid-1970s, progress in electronics and photonics has introduced novel materials and devices, enabling the exploration of the THz gap to become a subject of considerable interest in recent years. It holds great promise for fundamental physics and diverse fields, including imaging [1], communications, security, and a wide variety of applications [2]. Recently, the generation of THz radiation varies across materials, with each substance exhibiting unique properties in emitting these waves. Different materials play a crucial role in influencing and shaping THz generation processes. The generation of THz radiation in lithium niobate ($LiNbO_3$ or LN) and lithium tantalate ($LiTaO_3$ or LN) has been a subject of significant interest and research. These materials, belonging to the trigonal crystal system, have unique properties for THz generation. LN, for instance, has been widely used in diverse applications, including the efficient generation of high-field THz pulses [3]. Similarly, LT has been studied for its potential in coherent tunable THz generation [4]. The unique crystal structures and optical properties of these materials make them suitable for generating and manipulating THz radiation. One of the most prominent techniques for generating THz pulses within the 0.1 to 2 THz frequency range involves a process called optical rectification (OR). This method uses femtosecond near-infrared laser pulses to interact with a crystalline material, such as LN, leading to the generation of both high-energy broadband THz pulses [5-7] and narrowband radiation [8-10]. The success of OR can be attributed to several critical factors. The nonlinear tensor responsible for OR is directly related to the refractive indices, and the choice of materials and phase-matching schemes can significantly impact the efficiency of the process. One key element is the substantial difference in the indices of refraction between the near-infrared laser light used for pumping and the THz waves. The difference between the refractive indices should be minimized to enable efficient conversion of the pump energy into THz radiation however the conversion efficiency is influenced by various factors, including the properties of the material used and the characteristics of the optical pulse [11]. The process of quasi-phase matching, achieved through periodic poling of the crystalline material [12], as well as velocity matching

through tilted-pulse-front pumping [13], plays an important role in enhancing the conversion efficiency for both narrowband and broadband pulse generation. Tilted pulse front pumping has enabled efficient velocity matching in LN crystals renowned for their high damage threshold and nonlinear coefficient [14]. According to [15], THz generation efficiencies of approximately 3% and 1% are predicted for LN and LT, respectively. However, the nonlinear absorption phenomenon poses a significant challenge to optical frequency conversion processes, such as OR, due to its potential to reduce efficiency. This phenomenon encompasses multi-photon absorption (MPA) [16,17] and free-carrier absorption (FCA) [17], which have been observed in various materials [18]. Nonlinear frequency conversion, a parametric process, is susceptible to these mechanisms, which can lead to a strong negative impact on the efficiency of the conversion process [18]. Nonlinear optics, which governs these phenomena, explains the nonlinear response of properties such as frequency, polarization, phase, or path of incident light. It gives rise to a variety of optical phenomena, including frequency-mixing processes like second harmonic generation (SHG) and third harmonic generation (THG). These nonlinear absorption mechanisms have significant interest due to their potential to exert a strong negative impact on the efficiency of frequency conversion processes. In nonlinear optical frequency conversion applications, such as OR, LN crystal may exhibit MPA and nonlinear refraction effects at high laser intensities. Several studies have been conducted on the determination of MPA coefficients in LN and LT crystals using different techniques. However, the Z-scan setup originally introduced by Sheik-Bahae et al [19] is a reliable and accurate method for measuring MPA coefficients in these materials. This technique involves measuring the transmission of a material as a function of the beam's position along the optical axis. A simple transmission measurement was used to determine the 2PA [20] in LN. However, the Z-scan technique was applied to evaluate the 3PA in LN [21] and used to investigate the scanning nonlinear absorption in LN over the time regime of small polaron formation [22]. Notably, to the best of current knowledge, 4PA of LN has not yet been measured using the Z-scan technique. In previous attempts, the 4PA coefficient of LN was estimated based on the saturation of THz pulse generation efficiency with increasing pump intensity [23]. Recently, a simple transmission measurement was used to determine the 4PA coefficient of stoichiometric LN [24]. In the case of LT 2PA coefficient and third-order nonlinear refractive index were

determined using the Z-scan setup [25]. Another study investigated 2PA in undoped lithium tantalate crystals [26] and congruent crystals [27]. While 3PA coefficients have not been determined yet. These investigations into the nonlinear optical properties of LN and LT are crucial for understanding and optimizing its performance in a range of applications.

The research aimed to determine the 3PA in both LN and LT crystals at 800 nm and 4PA in LN at 1030 nm of central wavelength using open aperture Z-scan technique. The dependence of the MPA on the Mg doping concentration and at different intensity levels were also investigated for both ordinary and extraordinary polarized light. 3PA and 4PA coefficients of these crystals were numerically determined from the measured Z-scan curves. Knowledge of these MPA coefficients is crucial for the accurate design and optimization of frequency conversion, electro-optical, and other photonic devices working in both the infrared and THz ranges.

1.2 Dissertation Outline

In this thesis, I delve into the determinations of nonlinear optical properties of crystals, specifically focusing on LN and LT.

This thesis will discuss the following within their chapters: In the introductory chapter, I present the background and motivation behind our research and set the stage for the dissertation outline. Chapter Two consists of the properties of the examined materials (LN and LT). Chapter Three delves into the nonlinear optical properties, discussing the MPA, free carrier absorption, and other interactions between light and matter, such as second harmonic generation and coherence length. Chapter Four introduces the Z-scan technique as the main method for our research and their interpretations in both closed-aperture and open-aperture configurations, including the description of the Gaussian beam, and the knife-edge method. Moreover, it also discusses the determination of refractive index and absorption coefficients and the numerical model used for the evaluation of multiphoton absorption coefficients in LN and LT crystals. Chapter Five consists of the motivation behind the work and outlines the research objectives. Moving on to Chapter Six, I detail the materials and methods employed, specifically the Z-scan setup for 800 nm and 1030 nm lasers, beam radius measurements, sample preparation, and the UV absorbance spectra for all investigated crystals. Chapter Seven presents the results of the experimental work, showing the Z-scan curves obtained for both laser

wavelengths, 800 nm, and 1030 nm, with a specific focus on LN and LT. Chapter Eight is dedicated to the discussion of the findings of the multiphoton absorption in LN and LT and drawing comparisons between the two. In Chapter Nine, I draw the work to a conclusion. Chapter Ten provides the thesis statements that summarize the main findings and contributions of this thesis. Chapter Eleven and Twelve contain the summaries of my study.

Chapter Two: Properties of the Examined Materials

2.1 Lithium niobate

LN has become a prominent choice for technological applications in both electro-acoustic and electro-optical domains. Its remarkable and notably expansive properties [28,29] find practical utility across a wide spectrum of applications. Consequently, LN stands out as a focal point in the realm of ferroelectric research [30–32]. Over the past five decades, the effort of the ferroelectric community has yielded unparalleled insights into the underlying physical mechanisms that govern the material's attributes. LN was first fabricated in Bell Laboratories in the mid-'60s. It is a colorless solid, insoluble in water. It is transparent for wavelengths between 320 and 5200 nm. LN possesses a trigonal crystal structure [33] and features a relatively large bandgap of around 3.8 eV [34,35]. These properties are crucial in making LN suitable for nonlinear optical applications. As a non-centrosymmetric crystal, it exhibits negative uniaxial birefringence behavior. Due to its diverse range of properties and practical applications, this material has been extensively investigated in research [36,37]. LN does not occur naturally. The fabrication of LN involves the growth of crystals from a melt composed of lithium oxide (Li_2O) and niobium oxide (Nb_2O_5). The process of growing LN crystals is typically achieved through methods such as the Czochralski method which involves pulling and rotating a seed crystal while the growing crystal is in contact always with the surface of the melt [38]. Since Nb ions tend to substitute for Li ions during crystal growth, it is necessary to maintain a homogeneous crystal with a consistent composition. This is achieved through the use of a "congruent melt", which contains 48.45 mol% Li_2O and 51.55 mol% Nb_2O_5 [39]. Nevertheless, the cLN crystal is characterized by a significant presence of intrinsic defects, specifically Nb anti-sites (Nb_{Li5+}) and lithium vacancies (V_{Li-}), thereby restricting its suitability for optical applications [40,41]. In recent years, stoichiometric LN (sLN) with excellent homogeneity has become available as well. sLN single crystals exhibit numerous improved properties. These include reduced damage resistance when compared to congruent ones, enhanced electro-optic coefficients, a shorter absorption edge wavelength, and a lower electric field threshold for ferroelectric domain switching compared to conventional congruent LN single crystals [42]. Doping LN with magnesium oxide (Mg:LN) enhances its resistance against optical damage [43]. Notably, the concentration of MgO required for achieving this effect is lower in

Mg:sLN than in Mg:cLN [44,45]. For cLN, a doping level of over 5 mol% Mg is required to suppress photorefraction, while for sLN, a lower doping level of about 0.6 mol% Mg is sufficient. In terms of its nonlinear optical properties, at 1030 nm it demonstrates a high damage threshold of 204 GW/cm^2 for 1 ps pulses, operating at a repetition rate of 10 kHz, and with a threshold intensity of 2.4 TW/cm^2, and 330 fs, and with a repetition rate of 20 kHz [46]. Additionally, it has a high nonlinear coefficient, which strongly depends on the material's constituents [47]. It exhibits a notable nonlinear optical coefficient of around 30 pm/V for frequency conversion processes in the near-infrared range [33]. Furthermore, it presents a fascinating value of 160 pm/V for the OR process [48]. This property is crucial for nonlinear optical applications, as it determines the efficiency of nonlinear processes such as frequency conversion and harmonic generation. In terms of its structure, LN belongs to the trigonal space group R3c (below the Curie temperature at about 1130 °C). The hexagonal unit cell is depicted in Figure 2-1, including the hexagonal axes *a*, *b*, *c* and the axes of the cartesian crystal coordinate system *X*,*Y*, *Z*. The cations Li^+ and Nb^{5+} are displaced along the *Z* axis with respect.

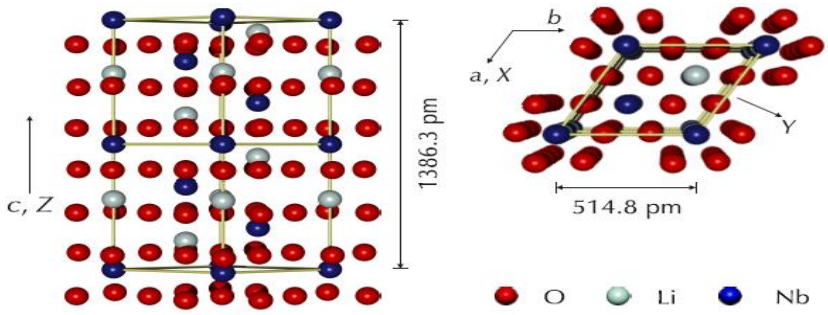

Figure 2-1: Crystal structure of $LiNbO_3$ [49].

Ferroelectric crystals like LN also present various distinctive properties, encompassing both optical and electrical aspects. These encompass effects such as pyroelectric, piezoelectric, photoelastic, photovoltaic, electro-optic, and photorefractive effects [50], alongside optical nonlinearity. Frequently, these properties interrelate and can co-exist within a single process. For instance, the photorefractive effect emerges from the synergy between photovoltaic and electro-optic effects. LN's prominence in optics research arises from its substantial electro-optic and nonlinear coefficients, denoted as r_{ijk} and d_{ijk}, respectively. LN displays a pyroelectric effect along the polar axis only, meaning that the pyroelectric first-order tensor has a single non-zero coefficient. This

is caused by the rearrangement of the Li and Nb ions relative to the oxygen octahedra wherein an increasing temperature reduces both the ion displacement and the resultant spontaneous polarization [50]. This change in polarization can be detected by the flow of charge to and from the surface. This polarization shift is discernible through charge movement to and from the surface. The third-rank tensor for optical nonlinearity, d_{ijk}, comprises 27 coefficients. In cases where dispersion can be overlooked, applicable solely in situations far from material resonances, thereby existing in a lossless domain, the Kleinman symmetry condition [51] dictates that d remains invariant upon permutation of indices i, j, k illustrated by examples like $d_{122} = d_{212} = d_{221}$. Consequently, the original 27 coefficients of the d tensor can be condensed to 10 independent elements. Symmetries dictated by the 3m crystal class further contribute to coefficient reduction. In general, the nonlinear tensor d consists of 18 elements in the contracted notation. If the crystal structure and its symmetries are taken into account, some tensor elements may be zero or some elements equal to other ones:

$$d = \begin{pmatrix} 0 & 0 & 0 & 0 & d_{31} & -d_{22} \\ -d_{22} & d_{22} & 0 & d_{31} & 0 & 0 \\ d_{31} & d_{31} & d_{33} & 0 & 0 & 0 \end{pmatrix}$$

In a research investigation, Shoji and colleagues [52] derived numerical values corresponding to the coefficients d_{33} and d_{31}. The value of d_{22} is notably smaller than that of d_{31}, as reported in a previous study [53], which consequently limits its practical utility. The determination of values for different wavelengths can be achieved through the application of Miller's rule [54], although the reliability of this rule has been questioned in light of subsequent findings [52].

2.2 Lithium tantalate

LT shares similarities with LN as an optical crystal [55] and an isomorphic relationship, where the Nb^{5+} ion is substituted by the Ta^{5+} ion [56] with a relatively large band gap of 4.9 eV [57], playing a vital role in devices that exploit its bulk [58] and surface properties. Below the Curie temperature at about 630 °C, LT crystallizes in the R3c space group, mirroring LN [59,60]. Beyond this temperature, it adopts the R-3c space group [61,62]. It is an important ferroelectric material used in various applications [63], such as acoustic- and optoelectronics, frequency modulators, transducers, and nonlinear optics owing to its wide transparency range (0.27–6 μm), large nonlinear coefficients

[64], and high resistance to optical damage [65]. It is a material of interest and promising in terms of THz generation through nonlinear optical processes also due to its excellent optical and electronic properties [66], large nonlinear coefficients, and high damage thresholds. The growth process with a rich combination of ferroelectric, pyroelectric, nonlinear optical, and piezoelectric properties [67-72] of LT is similar to that of LN forming a congruent material cLT through the conventional Czochralski method. While properties of structurally and electronically similar ferroelectric crystals such as LN and LT exhibit minor distinctions. The crystal structure of LT is shown in Figure 2-2 [26,76]. This structure generates a spontaneous polarization *Ps* of approximately 50 μC/cm². It's worth noting that, unlike LN which has a melting point of 1235°C and a Curie temperature of 77 °C, LT boasts a higher melting point of 1650°C, but its Curie temperature is significantly lower at 600°C. This decrease in Curie temperature holds significance for the fabrication of domain-engineered devices. Processes such as in diffusion for waveguide creation might elevate the crystal's temperature beyond the Curie point, leading to the disintegration of its domain structure. Just as in LN, there's a growing interest in developing stoichiometric lithium tantalate sLT materials. Because of their analogous structures, many properties exhibited by LN are qualitatively replicated in LT. Indeed, several values even match quantitatively [73]. Consequently, many of the previously discussed aspects are pertinent to both materials. The material's transmission spectrum closely resembles that of LN. LT shares similar optical nonlinear coefficients and photorefractive optical damage thresholds (ODT) as LN. Similarly, LT also displays augmented photoconductivity, leading to a reduced saturation photorefractive index change with increased Li content [74]. Researchers have successfully created periodically poled sLT, enabling blue SHG. Intriguingly, this process demonstrates no photorefractive damage when subjected to input power exceeding 1 W/cm^2 at room temperature [75].

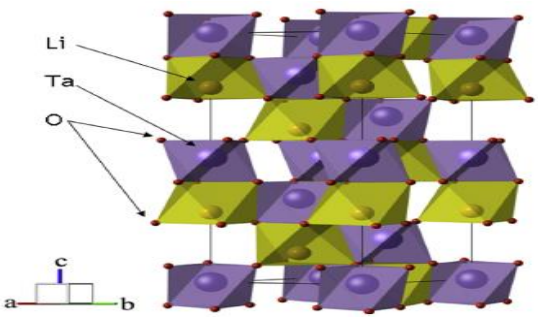

Figure 2-2: Crystal structure of $LiTaO_3$ [26,76].

Chapter Three: Nonlinear Optical Properties

Nonlinear optics is a field of optics that deals with the interactions between light and matter in situations where the response of the material is not proportional to the intensity of the light. The inception of the nonlinear optics field is commonly attributed to the identification of SHG in 1961 by Franken et al. [77], which occurred shortly after Maiman's successful demonstration of the first operational laser in 1960 [78]. In linear optics, the behaviour of light-matter interactions follows the principles of superposition, meaning that the effects caused by different light waves simply add up. In nonlinear optics, however, the relationship between the incident light and the effects becomes more complex due to higher-order interactions. In a linear, homogeneous, and isotropic medium, the polarization is linearly proportional to the electric field [79]. As a femtosecond laser pulse propagates through a nonlinear material, it causes a time-dependent polarization change, leading to the emission of electromagnetic radiation. The scalar relationship between the polarization P, linear electric susceptibility χ, and electric field E of the femtosecond laser pump radiation can be written as

$$P(t) = \epsilon_o \chi E(t) \tag{3- 1}$$

This indicates that the material's polarization is proportional to the electric field. Besides the linear process, the nonlinear material also experiences nonlinear processes. These processes can be described by expanding χ in powers of the field E as illustrated by Eq. (3-2).

$$\begin{aligned} P(t) = P^{(1)} + P^{(2)} + P^{(3)} + \cdots \\ = \epsilon_o(\chi^{(1)}E + \chi^{(2)}EE + \chi^{(3)}EEE + \chi^{(4)}EEEE \\ + \chi^{(5)}EEEEE + \chi^{(6)}EEEEEE + \cdots) \end{aligned} \tag{3- 2}$$

where $\chi^{(2)}$ and $\chi^{(3)}$ are the second-and third-order nonlinear susceptibilities, respectively. The time-varying polarization $P(t)$ acts as a source of new components of electromagnetic fields. The associated wave equation governing electromagnetic radiation propagation in the nonlinear optical medium is of the form

$$\nabla^2 E - \frac{n}{c^2}\frac{\partial^2 E}{\partial^2 t} = \frac{1}{c^2 \epsilon_o}\frac{\partial^2 P_{nl}}{\partial^2 t} \tag{3- 3}$$

where n is the linear refractive index of the material.

3.1 Multi-photon absorption

Absorption mechanisms exhibit pronounced non-linearity, especially in the vicinity of atomic resonances. Considering a non-linear form of Beer's law, alterations in intensity along distance *z*. The absorption coefficient α can be either larger or smaller with increasing intensity, contingent upon the underlying physical phenomenon. Increasing absorption, even within transparent mediums, arises from the introduction of multi-photon absorption at high intensities. Conversely, reduced absorption arises from the saturation of the absorption line due to intense light exposure. When considering absorption, the well-known Beer's law applies to linear absorption defined as:

$$I(z) = I_0 e^{-\alpha z} \tag{3- 4}$$

where I_0 is the incident intensity, α is the linear absorption coefficient, z is the propagation depth in the absorbing medium and $I(z)$ is the intensity at depth z. Beer's law is merely the solution of the differential equation that describes how light intensity decreases with propagation depth in a medium for the case where α is a constant,

$$\frac{dI(z)}{dz} = -\alpha I(z) \tag{3- 5}$$

If nonlinear (multi-photon) effects are to be included then this differential equation must be extended to include higher-order intensity terms [23],

$$\frac{dI(z)}{dz} = -\alpha I(z) - \beta I^2(z) - \gamma I^3(z) - \delta I^4(z), \tag{3- 6}$$

where β is the two-photon absorption coefficient (2PA), γ is the three-photon absorption coefficient (3PA) and δ represents the four-photon (4PA) and higher absorption terms.

In the expression for the polarization in *Eq* (3-2), The lowest-order nonlinear absorption is described by the imaginary part of the $\chi^{(3)}$ which corresponds to 2PA. The imaginary part of $\chi^{(5)}$ relates to 3PA. Now, an attempt is made to derive the relation between the 2PA and 3PA coefficients and the imaginary part of the third- and fifth-order susceptibility. In the presence of a monochromatic field, the polarization is given by

$$P(t) = \epsilon_o(\chi^{(1)} E\cos(\omega t) + \chi^{(3)}(E\cos(\omega t))^3 + \chi^{(5)}(E\cos(\omega t))^5 \dots) \quad (3\text{-}7)$$

The polarization contains components oscillating at frequencies ω, 3ω, 5ω and higher harmonics whereas the applied electric field oscillates at frequency ω. Neglecting the higher-order nonlinearity and also higher harmonic terms in *Eq* (3-2) will lead to the following.

$$P_\omega^{(1)}(t) = \epsilon_o(\chi^{(1)} + \frac{3}{4}E^2\chi^{(3)} + \frac{5}{8}E^4\chi^{(5)})\, E\cos(\omega t) \quad (3\text{-}8)$$

The effective first order susceptibility is now modified such that it contains two additional terms arising from the third- and fifth-order nonlinearity. Therefore, the complex refractive index is now given by

$$n = \sqrt{1 + \chi_{eff}^{(1)}} = \sqrt{1 + \chi^{(1)} + \frac{3}{4}E^2\chi^{(3)} + \frac{5}{8}E^4\chi^{(5)}} \quad (3\text{-}9)$$

The real part of susceptibility relates to the index of refraction whereas the imaginary part relates to the absorption coefficient. Therefore, the complex refractive index can be written as

$$n = \sqrt{\left(1 + \chi_R^{(1)} + \frac{3}{4}E^2\chi_R^{(3)} + \frac{5}{8}E^4\chi_R^{(5)}\right) + i\left(\chi_I^{(1)} + \frac{3}{4}E^2\chi_I^{(3)} + \frac{5}{8}E^4\chi_I^{(5)}\right)} \quad (3\text{-}10)$$

The imaginary part of the complex refractive index is always smaller than its real part allows us to separate the real and imaginary parts of the complex refractive index using the following approximation.

$$n = n_R + in_I = \sqrt{\left(1 + \chi_R^{(1)} + \frac{3}{4}E^2\chi_R^{(3)} + \frac{5}{8}E^4\chi_R^{(5)}\right)} + i\frac{\left(\chi_I^{(1)} + \frac{3}{4}E^2\chi_I^{(3)} + \frac{5}{8}E^4\chi_I^{(5)}\right)}{2\sqrt{\left(1 + \chi_R^{(1)} + \frac{3}{4}E^2\chi_R^{(3)} + \frac{5}{8}E^4\chi_R^{(5)}\right)}} \quad (3\text{-}11)$$

The imaginary part of the complex refractive index can be written as:

$$n_I = \frac{\chi_I^{(1)} + \frac{3}{4}E^2\chi_I^{(3)} + \frac{5}{8}E^4\chi_I^{(5)}}{2\sqrt{\left(1 + \chi_R^{(1)}\right)}} = \frac{\chi_I^{(1)}}{2n_0} + \frac{3\chi_I^{(3)}I}{4n_0^2c\varepsilon_0} + \frac{5\chi_I^{(5)}I^2}{4n_0^3c^2\varepsilon_0^2} \quad (3\text{-}12)$$

For example by supposing: α_0, α_2 and α_3 are linear absorption coefficient, 2PA and 3PA coefficients respectively. However, the absorption coefficient is connected to the imaginary part of the complex refractive index through the following relation

$$\alpha(I) = \frac{2\omega}{c} n_I = \alpha_0 + \alpha_2 I + \alpha_3 I^2 \quad (3\text{- }13)$$

where the linear absorption coefficient is defined as:

$$\alpha_0 = \frac{\omega \chi_I^{(1)}}{c n_0} \quad (3\text{- }14)$$

Comparison between Equations (3-12) and (3-13) allows one to determine the relation between nonlinear absorption coefficients and nonlinear susceptibilities as given in Equations (3-15) and (3-16).

The 2PA coefficients contains the oscillating frequency ω, and is identified as:

$$\alpha_2 = \frac{3\omega}{2 n_0^2 c^2 \varepsilon_0} \chi_I^{(3)} \quad (3\text{- }15)$$

The 3PA coefficients defined as the probability of simultaneous absorption of three photons at frequency ω is obtained as:

$$\alpha_3 = \frac{5\omega}{2 n_0^3 c^3 \varepsilon_0^2} \chi_I^{(5)} \quad (3\text{- }16)$$

3.2 Free carrier absorption

In the case of semiconductor material, photon absorption is directly proportional to the carrier densities within the material. This relationship is a consequence of the interaction between photons and charge carriers, such as electrons and holes. When a photon with sufficient energy is absorbed by a semiconductor, it can promote an electron from the valence band to the conduction band, creating an electron-hole pair. The possibility of this process occurring is determined by the availability of carriers, as a higher carrier density increases the chances of a photon finding an available carrier to interact with. Therefore, the rate of photon absorption in a semiconductor is directly linked to the carrier density, making carrier concentrations a critical factor in understanding and controlling the optical properties of semiconductor devices. In the case of THz generation, previous studies have indicated one of the main limitation

factors on the THz conversion efficiency is the free-carried absorption (FCA) induced by multi-photon absorption [80].

The free-carrier density (n_{fc}) generated by the incident pump pulse can be calculated from *Eq*. (3-13) [23,81].

$$n_{\mathrm{fc}} = \frac{I\tau}{hc/\lambda_o}\left(\alpha + \frac{1}{2}\beta I + \frac{1}{3}\gamma I^2 + \frac{1}{4}\delta I^3 + \cdots\right) \qquad (3\text{-}17)$$

where I is the pump intensity, τ is the pulse duration, h is the Planck's constant, $\lambda_o = 2\pi c/\omega_o$ is the pump central wavelength, α is the linear absorption, β, γ, and δ are the two-, three-, and four-photon absorption coefficients, respectively. The FCA coefficient (α_{fc}), can be calculated from the Drude model as:

$$\alpha_{fc}(\Omega) = \frac{2\Omega}{c}\Im m\sqrt{\varepsilon_\infty.\left(1 - \frac{\omega_p^2}{\Omega^2 + i\Omega/\tau_{sc}}\right)} \qquad (3\text{-}18)$$

where ε_∞ is the high-frequency dielectric constant, $\omega_p^2 = e^2 n_{\mathrm{fc}}/(\varepsilon_o \varepsilon_\infty m_{\mathrm{eff}})$ is the plasma frequency, e is the electron charge, m_{eff} is the effective mass, and τ_{sc} is the electron scattering time.

3.3 Other interaction between light and matter and related phenomena

3.3.1 Second harmonic generation

The process of SHG is illustrated schematically in Figure 3-1, it occurs as a second-order nonlinear phenomenon resulting from the interaction of light within nonlinear optical media. Discovered by Franken in 1961[82]. SHG is a specific nonlinear optical process in which two photons of the same frequency combine to generate a single photon with twice the frequency and therefore half the wavelength of the input photons.

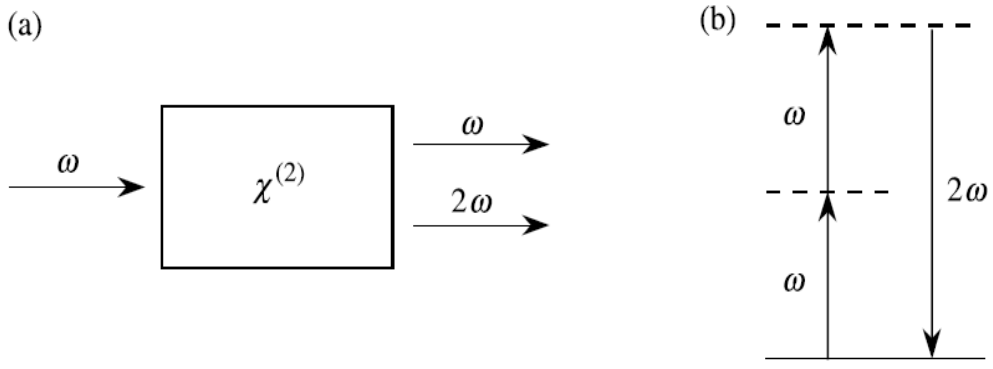

Figure 3-1: (a) Geometry of SHG. (b) Energy-level diagram describing SHG [83].

The electric field $E(r,t)$ is defined locally at a position r and time t. A plane monochromatic wave incident on the material is described by

$$E(r,t) = \frac{1}{2}\left(E(r)e^{-i\omega t} + c.c.\right) \tag{3-19}$$

where *c.c.* is the complex conjugate of the preceding term. Substituting *Eq*. (3-15) into *Eq*. (3-4) we obtain:

$$P(r,t) = \varepsilon_0 \frac{1}{2}\left[\chi^{(1)}\left(E(r)e^{-i\omega t} + c.c.\right)\right] + \varepsilon_0 \left[\chi^{(2)}E(r)\left(E(r)\right)^* + \frac{1}{2}\left(\chi^{(2)}\left(E(r)\right)^2 e^{-2i\omega t} + c.c.\right) + \cdots\right] \tag{3- 20}$$

The first term is the polarization component arising from the linear response of the medium to the applied field, and the second term of *Eq*. (3-16) describes the second-order polarization and arises from the quadratic nonlinear response of the medium.
When the field *Eq*. (3-15) is incident upon a material with a nonzero second-order susceptibility $\chi^{(2)}$, the nonlinear polarization $P(r,t)^{(2)}$ created in the material is described by *Eq*. (3-17).

$$P^{(2\omega)}(r,t) = 2\varepsilon_0\chi^{(2)}E(r)\left(E(r)\right)^* + \left(\varepsilon_0\chi^{(2)}\left(E(r)\right)^2 e^{-2i\omega t} + c.c.\right) \tag{3- 21}$$

Where the first term describes the optical rectification phenomenon. Another contribution to the polarization is created at a frequency 2ω (second term) and describes the coherent radiation of a photon with a frequency 2ω, a process called SHG.

3.3.2 Coherence length

As described above, the SHG nonlinear optical process where only two waves are involved, the fundamental (pump) beam at frequency $\omega_{inc} = \omega$ and the SHG wave $\omega_{SHG} = 2\omega$. Phase matching of these two waves in *k*-space is required [84].

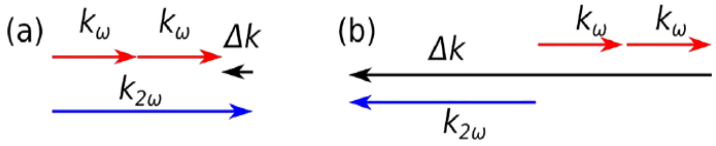

Figure 3-2: Vector diagrams for the SHG process for (a) co- and (b) counter-propagating beams [84].

$$2k_\omega - \Delta k = \pm k_{2\omega}, \tag{3- 22}$$

where Δk is the phase mismatch.

According to $2\pi n_\omega/\lambda_\omega$ with n_ω is the refractive index at a given wavelength λ_ω, and $\Delta k = \pi/l_c,\ l_c$ is defined as [85]:

$$l_c = \frac{\pi}{\Delta k} = \frac{\lambda_\omega}{4}\frac{1}{n_{2\omega} \pm n_\omega} \tag{3-23}$$

The coherence length l_c is directly related to SHG in nonlinear optics. In the context of SHG, the coherence length represents the maximum distance over which the second harmonic signal can build up coherently before it undergoes destructive interference and back-conversion to the fundamental frequency. To be more precise, l_c is the distance over which SHG at a certain point in the medium still adds constructively with SHG at a distance l earlier in the medium. Due to dispersion in the medium, SHG may propagate with a different phase velocity compared to the fundamental frequency. After a certain distance (*Eq.* (3-19)), the second harmonic will add destructively with the previously generated second harmonic, leading to back-conversion. The coherence length is crucial for the efficient generation and propagation of second harmonics. If the medium's length is less than the coherence length, constructive interference occurs, and the second harmonic builds up. However, beyond the coherence length, destructive interference dominates, and the second harmonic signal decreases. The coherence length is a critical factor in determining the maximum thickness of a crystal that can be efficiently employed in optical processes, such as enhancing THz generation and detection efficiency.

Chapter Four: Z-scan Technique

4.1 Tool for method: Gaussian beam, Knife edge method

4.1.1 Gaussian beam

Gaussian beams, characterized by their unique intensity distribution and propagation characteristics, are one type of collimated beams. These beams, often used in various applications, can be rigorously examined and analyzed through multiple methods. One such method involves the utilization of the paraxial wave equation [86], which offers a comprehensive framework for understanding the behaviour of Gaussian beams. Additionally, Gaussian beams can also be investigated by applying the principles of Fourier optics, a powerful mathematical approach that represents the electric field as a complex and expansive plane wave spectrum [87] as well described in reference [88]. To characterize a beam, it is necessary to establish its radius. It's worth noting that the double of this radius corresponds to the beam diameter which is usually referred to as the spot size. Given the Gaussian distribution across the transverse plane, a specific distance from the central axis must be chosen, at which the intensity reaches a designated proportion of the intensity at the optical axis. Several options exist for this selection including utilizing the distance at which the intensity decreases to one-half, resulting in the known full width at half maximum (FWHM). Opting for a distance that is twice the standard deviation of the Gaussian profile. Employing distances where the intensity drops from one peak fraction to another this definition is closely related to the knife-edge measurement as will be further explained. The beam radius is the distance from the beam axis where the optical intensity drops to $1/e^2$ corresponding to 13.5% of the value on the beam axis. In this instance, the value is calculated as $2w_{1/e^2} \approx 1.699$ FWHM. This method stands out as one of the most commonly used methods. Allowing the point's distance from the optical axis to be $r = \sqrt{x^2 + y^2}$, and the distance of the projection of the point to the axis from the beam waist position to be z, the intensity will be given by:

$$I(r,z) = I(0,z)e^{-\frac{2r^2}{w(z)^2}} \tag{4- 1}$$

The characteristics and parameters that define a Gaussian beam are: Beam radius, radius of curvature, and Gouy phase shift numbered in order respectively:

$$w(z) = w_0\sqrt{1 + \left(\frac{z}{z_R}\right)^2} \tag{4- 2}$$

and the radius of curvature of the wavefronts *R(z)*:

$$R(z) = z\left[1 + \left(\frac{z_R}{z}\right)^2\right] \tag{4- 3}$$

and the phase factor (often referred to as Gouy's phase) takes the form:

$$\varphi_G(z) = tan^{-1}\left(\frac{z}{z_R}\right) \tag{4- 4}$$

The Rayleigh range corresponds to the distance from the beam waist where the intensity becomes half of what it is at the waist and that as a direct consequence,$w(z_R) = w_0\sqrt{2}$.

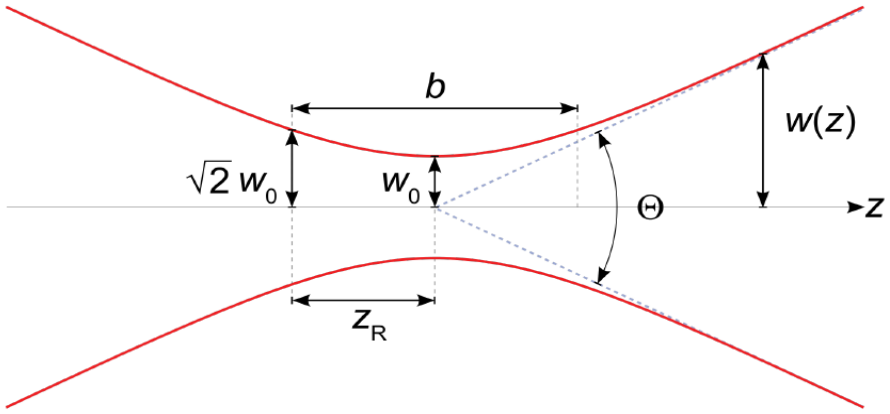

Figure 4-1: Gaussian beam parameters associated with beam waist(w_0), Rayleigh length (z_R), and angular divergence [89].

Furthermore, the depth of focus parameter, noted as *b* is twice the Rayleigh length, placing its midpoint at the beam waist position z_0. Another important parameter is the beam divergence, which is defined as:

$$\theta = \lim_{z\to\infty} arctan\left(\frac{w(z)}{z}\right). \tag{4- 5}$$

In the paraxial conditions, would yield

$$\theta = \frac{\lambda}{\pi w_0}. \tag{4- 6}$$

Gaussian beams can also be described by the complex beam parameter *q(z)*:

$$q(z) = z + iz_R. \tag{4- 7}$$

We can separate the real and imaginary parts of this parameter as

$$\frac{1}{q(z)} = \frac{1}{R(z)} - i\frac{\lambda}{\pi w_0^2} \tag{4- 8}$$

An optical element with a given ABCD ray transfer matrix will change the beam parameter to

$$q'(z) = \frac{Aq + B}{Cq + D} \tag{4- 9}$$

In terms of Gaussian spatial intensity distribution:

Determining the peak intensity along the optical axis holds a large significance. To achieve this, examine a consideration where a power of *P* is directed onto a circular area with a radius of *r*. Assuming a Gaussian distribution, approach the limit by reducing this circular area to a point, resulting in:

$$I_p(0,z) = \lim_{r\to 0} \frac{P\left(1 - e^{\frac{-2r^2}{2w^2}}\right)}{\pi r^2} = \frac{2P}{\pi w^2} \tag{4- 10}$$

This crucial finding, which states that the peak intensity equals twice the average intensity, essentially the straightforward ratio of power to area is a fact that is occasionally overlooked, and yet it can lead to substantial issues.

$$I_{peak} = 2\frac{P}{A} = \frac{2P}{\pi w_0^2} \tag{4- 11}$$

We should also give the intensity along the optical axis, which, considering *Eq*. (4-2) will be

$$I(0,z) = \frac{I(0,0)}{1 + \left(\frac{z}{z_R}\right)^2} \tag{4- 12}$$

To conclude regarding the Gaussian beam intensity at any point, we can now express it through the power as

$$I(r,z) = \frac{2P}{\pi w_0^2 \left[1 + \left(\frac{z}{z_R}\right)^2\right]} e^{-\frac{2r^2}{w_0^2\left[1+\left(\frac{z}{z_R}\right)^2\right]}} \quad (4\text{- }13)$$

The above description, however, does not represent real beams. Real beams have astigmatism: that is, the perpendicular components *x* and *y* do not propagate the same way. This means that the position of the beam waist (z_0) the waist radius (w_0) the Rayleigh range (z_R) are all different for the two components.

The Gaussian distribution can be assumed for each of the two components. In this case, we will have to express *Eq*. (4-1) as

$$I(x,y,z) = I(0,0,z) e^{-\frac{2x^2}{w_x^2(z)}} e^{-\frac{2y^2}{w_y^2(z)}} \quad (4\text{- }14)$$

The peak intensity described in *Eq*. (4-11), neglecting that the beam waist for the two components can be in different positions $z_{0x} \neq z_{0y}$ will be defined as:

$$I_{peak} = \frac{2P}{\pi w_{0x} w_{0y}} \quad (4\text{- }15)$$

In terms of Gaussian temporal intensity distribution:

Pulses are Gaussian in the time; therefore, the correct equation is the following:

$$I(t) = I_{Peak} e^{-4\ln 2 \frac{t^2}{\tau^2}} \quad (4\text{-}16)$$

where τ is the FWHM of the Gaussian pulse. Additionally, it's worth observing that when we mention the calculated peak intensity, we are generally referring to the intensity at the beam waist, which will be defined as:

$$I_{Peak} = \frac{4E_l\sqrt{\ln(2)}}{\pi^{3/2}\tau w_{0x} w_{0y}} \quad (4\text{-}17)$$

The beam divergence, given by *Eq*. (4-5), in reality, is greater than that value and is equal only when the beam is perfectly Gaussian. We can thus define a parameter, that is a measure of "how Gaussian" a beam is by claiming:

$$w_0\theta_0 = M^2 \frac{\lambda}{\pi} \quad (4\text{- }18)$$

where the product of the waist radius and the divergence angle is called the Beam Parameter Product and $M^2$is simply referred to as the "M^2 factor". For theoretical that is purely Gaussian beams, this factor is unitary. For real beams, having a corresponding M^2 factor will allow us to treat the beams as if they are Gaussian. The difference now is that the beam radius will not be given as simply as in *Eq*. (4-2), but will [90]

$$w(z) = w_0\sqrt{1 + \left(\frac{M^2\lambda}{\pi w_0^2}\right)^2 (z - z_0)^2} \tag{4- 19}$$

From here, by taking into consideration the case when we calculate the radius at the Rayleigh length, knowing $w(z_R) = w_0\sqrt{2}$ we will get

$$\left(\frac{M^2\lambda}{\pi w_0^2}\right)^2 (z - z_0)^2 = 1 \tag{4- 20}$$

from which it is easy to determine

$$z_R = \frac{\pi w_0^2}{M^2\lambda} \tag{4- 21}$$

noting that throughout this work we are taking $z_0 = 0$ in all calculations. Thus, knowing how the M^2 parameter affects the beam divergence and the Rayleigh range, we now can describe even poorly Gaussian beams.

4.1.2 Knife-edge method

The knife-edge method is a very simple tool to measure the width of laser beams [91–94]. It consists of the propagation of a small non-transmitting screen, most commonly simply a knife edge, along the plane transversal to the propagation direction. While the knife edge propagates, the resulting change in the power transmitted is recorded, and the beam radius can thus be deducted. Has been commonly used to measure the beam diameter down to micrometres [95–97]. The principle of the knife-edge method is illustrated in Figure 4-2.

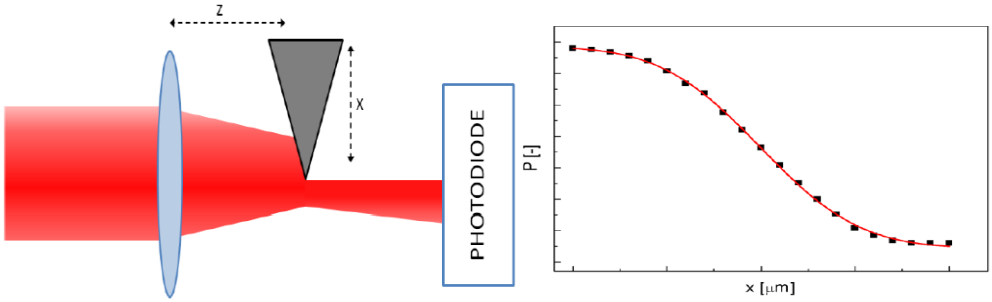

Figure 4-2: Principle of the knife edge measurement. b): The typical curve obtained during the measurement by the Knife Edge method [98].

Starting from a position where all the light is transmitted, and recording the power, to reach a certain level of transmittance, as described in the beginning of the Gaussian beams subsection, say, 90%. Then, having recorded the position, the knife edge is propagated until the power transmitted reaches 10% of the total, and the position is noted again. However, this method is not very precise, as the chance of having errors is present. Furthermore, this method does not give us any information on the shape of the distribution of the intensity that is we cannot tell if the distribution is Gaussian or not. Therefore, another method is used, which implements a fitting to determine the beam radius. Since the intensity distribution is assumed to be Gaussian, we can express the total power from the intensity given at *Eq.* (4-14) as [91].

$$P = I_0 \int_{-\infty}^{+\infty} e^{-\frac{2x^2}{w_x^2}} dx \int_{-\infty}^{+\infty} e^{-\frac{2y^2}{w_y^2}} dy = \frac{I_0 \pi w_x w_y}{2} \tag{4- 22}$$

The power transmitted as a function of the position x of the knife edge propagating orthogonally to the beam direction is given by

$$P(x) = \frac{P_0}{2}\left[1 \pm erf\left(\frac{x\sqrt{2}}{w_x}\right)\right] \tag{4- 23}$$

where the sign, positive or negative, is determined by the direction of propagation of the knife (out or into the beam). Thus, for a given position along the beam axis, having many measured pairs of the position of the knife edge and respective transmittance to find the corresponding beam radius.

4.2 Interpretation of Z-scan

Several methodologies are available for measuring the nonlinearity of optical materials, encompassing various advanced techniques. These methods play a crucial role in characterizing the behavior of materials under nonlinear optical conditions. Among these techniques, nonlinear interferometry, degenerate four-wave mixing and nearly degenerate three-wave mixing, ellipse rotation, and beam-distortion measurement stand out prominently [99]. These methods facilitate a comprehensive understanding of how the material's nonlinear response evolves across different frequency regimes. The z-scan technique is a well-established and widely used method for characterizing nonlinear absorption properties of materials. First introduced in 1990 by Sheik-Bahae [19] using a setup similar to the one shown in Figure 4-3, this technique involves recording the transmittance with the propagation of the sample under investigation along the focal point of a beam with a known intensity. There are two variations of this method: the closed-aperture Z-scan and the open-aperture Z-scan method for measuring the nonlinear index and nonlinear absorption coefficients, respectively. It's particularly useful for measuring coefficients related to 2PA and 3PA coefficients, etc., and other intensity-dependent absorption processes. This technique scans a focused laser beam through a sample along the Z-axis (propagation direction). The transmitted or reflected intensity is measured as a function of the sample position. The change in intensity provides information about the nonlinear absorption properties of the material. Here's how the Z-scan technique works and some of its key aspects.

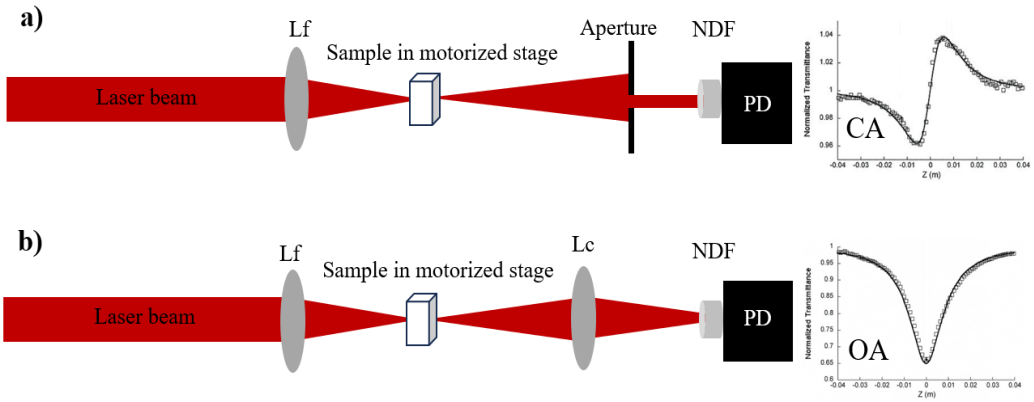

Figure 4-3: A schematic setup of closed aperture (a) and open aperture (b) Z-scan technique. Lf: focusing lens, Lc: collecting lend, NDF: neutral density filter, PD: photodiode [19].

4.2.1 Open-aperture

The standard open-aperture Z-scan technique involves directing a pulsed laser beam onto a sample using a lens. All energy passing through the nonlinear medium is collected using a lens and detected by a photodiode. The sample can be a solid or liquid and is moved through the focal point. The measured signal is recorded for each sample position, revealing how the nonlinear absorption coefficient varies with intensity. The resulting Z-scan trace is a V-shaped curve, with its depth correlating with the laser intensity at the focal point, sample thickness, and the sample's nonlinear absorption coefficient. In the absence of nonlinear absorption, the Z-scan signal forms a symmetric curve with either a minimum followed by a peak (positive self-lensing) or a peak followed by a valley (negative self-lensing). Positive nonlinearity leads to self-focusing, similar to a convex lens effect, where the medium focuses the laser beam. The laser intensity changes within the medium as it moves through the focal plane, acting as a variable focal length lens. As the sample moves towards the focus, self-focusing causes beam broadening and decreased transmittance, while moving away from the focus leads to beam narrowing and increased transmittance. Conversely, a medium with negative nonlinear refraction results in a Z-scan signal with a pre-focal peak followed by a post-focal valley. The Z-scan trace provides immediate information about the sign of the nonlinear refractive index.

4.3 Determining nonlinear refractive index and absorption coefficients

The accuracy of determining nonlinear coefficients such as nonlinear refraction γ or nonlinear absorption β depends on various factors, including competing nonlinearities, the nonlinearity model of the material, and the precise characterization of the laser source in terms of its temporal and spatial profiles, power or energy content, and stability [100]. The sign γ and β are readily obtained from Ref. [19]. In a thin nonlinear sample exhibiting cubic nonlinearity, the sample positioned at z exhibits a linear refractive index of n_o and a general refractive index n, which is a function of the irradiance $I(x, y, z)$. For a Kerr nonlinearity [19],

$$n = n_0 + \gamma I = n_0 + \frac{1}{2} n_2 |E|^2 \tag{4-24}$$

where n_0 is the linear index of refraction, E is the electric field amplitude within the sample (cgs), and I is the irradiance (MKS). The coefficient γ and n_2 are related through the conversion formula [19]

$$n_2(esu) = \frac{cn_0}{40\pi}\gamma(m^2W^{-1}) \tag{4-25}$$

Where c is the speed of light in a vacuum.

When the sample is thin and nonlinear, the beam doesn't have sufficient path length to change its size or shape as it moves through the medium. As a result of the nonlinearity, there is a phase change $\Delta\phi_o$ within the nonlinear medium.

$$\Delta\phi(r,z) = k\gamma I(r,z)L_{eff} \tag{4-26}$$

where k=2π/λ, λ is the wavelength, and L_{eff} is the effective sample length. $L_{eff} = (1 - e^{-\alpha_o L})/\alpha_o$, where L is the true sample length and α_o is the linear absorption coefficient. Here, the irradiance of a Gaussian beam, with waist size w_0 and waist at z = 0 as mentioned in *Eq*. (4.13)

$$I(r,z) = \frac{I_0 e^{-\frac{2r^2}{w(z)^2}}}{1 + \left(\frac{z}{z_R}\right)^2} \tag{4-27}$$

Where $w(z)$ is mentioned in *Eq*. (4-2), and the Rayleigh length is mentioned in *Eq*. (4-21). In this case, we will have to express *Eq*. (4-26) as:

$$\Delta\phi_0(0,z) \equiv k\gamma I(0,z)L_{eff} = \frac{\Delta\Phi_0}{1+\left(\frac{z}{z_R}\right)^2} \tag{4- 28}$$

where $\Delta\Phi_0 \equiv k\gamma I_0 L_{eff}$, and I_0 is the axial irradiance at the waist.

The nonlinearity can be assessed by comparing the maximum (peak) and minimum (valley) values of the normalized transmittance, which is denoted as $\Delta T = T_p - T_v$. The normalized transmittance, measured using an infinitesimal aperture at the observation plane, is given to first order in irradiance by a specific equation [101].

$$T = 1 - \frac{4\Delta\phi_0 v}{9+v^2} \tag{4- 29}$$

where υ is the linear phase $\upsilon = -\frac{1}{z_R}\left(z + \frac{{z_R}^2+z^2}{z_1-z}\right)$, if z_1 is much larger than z and z_R, then $\upsilon \approx -z/z_R$. For thin optical Kerr medium with nonlinear refractive index coefficient γ, ΔT is proportional to the nonlinear phase shift $\Delta\Phi o$ on the axis with the sample at the waist [19], and hence to γ:

$$\Delta T = 0.406|\Delta\Phi_0| \tag{4- 30}$$

Nonlinear absorption effects, including 2PA, can be incorporated by utilizing an absorption coefficient α that depends on the intensity of the irradiating light.

$$\alpha = \alpha_0 + \beta I = \alpha_0 + \alpha_2|E|^2. \tag{4- 31}$$

The nonlinear absorption coefficient β and α_2 are related by

$$\alpha_2(esu) = \frac{n_0 c}{8000\pi}\beta(mW^{-1}) \tag{4- 32}$$

The effect of the nonlinear absorption is to reduce the irradiance at the exit face of the sample to an amount $I_e(r,z)$.

$$I_e(r,z) = \frac{I(r,z)e^{-\alpha_0 L}}{1+\beta I(r,z)L_{eff}} \tag{4- 33}$$

The nonlinear phase shift associated with γ is reduced by the nonlinear absorption of the beam,

$$\Delta\phi_0(r,z) = \frac{k\gamma}{\beta}\ln\left(1+\beta I(r,z)L_{eff}\right) \tag{4- 34}$$

The determination of the nonlinear transmittance for simultaneous nonlinear refraction and absorption, monitored using a very small aperture, can be achieved [19].

$$T = \frac{1}{q_0}\ln(1+q_0) \tag{4- 35}$$

where q_0 is the on-axis absorption parameter $q_0 = \beta I(0,z)L_{eff} = \frac{Q_0}{1+\left(\frac{z}{z_R}\right)^2}$ and $Q_0 = \beta I_0 L_{eff}$. The coefficient of nonlinear absorption β can be evaluated using

$$\Delta T = \left|1 - \frac{1}{Q_0}\ln(1+Q_0)\right| \tag{4- 36}$$

Several factors can contribute to poor Z-scan profiles and unreliable data, including a weak input beam spatial profile, poor understanding of the temporal characteristics of the laser, fluctuating laser power, sample thickness, inappropriate size or distance, or poor alignment of the aperture for measuring on-axis transmittance, wedge and lens effects and other defects in the sample, and laser power exceeding the range of the low power regime. It is important to address these factors to ensure the accuracy and reliability of Z-scan measurements.

4.4 Evaluation of multiphoton absorption coefficients

4.4.1 Numerical model

To determine the β_n n^{th}-order MPA coefficient a pulse propagation model, similar to Ref. [102] was used. For every z_c position of the LN crystal, at the inner side of the entrance surface of the crystal, the following intensity distribution of the laser pulse was assumed:

$$I(z=0,x,y,t;z_c) = \frac{4n_0}{(n_0+1)^2} I_0 \frac{w_{0H}}{w_{0H}(z_c)} \frac{w_{0V}}{w_{0V}(z_c)} \exp\left(-\frac{2x^2}{w_{0H}^2(z_c)}\right) \exp\left(-\frac{2y^2}{w_{0V}^2(z_c)}\right) \exp\left(-\frac{4\ln(2)\,t^2}{\tau^2}\right) \tag{4-37}$$

Where $w_{0H,0V}(z_c) = w_{0H,0V}\sqrt{1+\frac{{z_c}^2}{z_{cRH,RV}^2}}$, τ is the FWHM duration of the laser pulse, and n_0 is the phase refractive index. The I_0 peak intensity of the laser beam at the beam-waist was calculated according to *Eq.* (4-38)

$$I_0 = \frac{4E_l\sqrt{\ln(2)}}{\pi^{3/2}\tau w_{0H} w_{0V}} \tag{4-38}$$

where E_l is the energy of the laser pulse before entering the crystal. The first term on the right side of *Eq.* (4-37) takes into account the reflection loss at the entrance surface.

The complex electric field envelope was determined inside the crystal at the beginning position as the following:

$$A(z=0,x,y,t;z_c)=\sqrt{\frac{2I(z_c,x,y,t)}{\varepsilon_0 c n_0}} \tag{4-39}$$

where ε_0 is the vacuum permittivity and c is the speed of the light in vacuum. For description of the pulse propagation inside the crystal,

$$\begin{aligned}&\frac{dA(z,x,y,t;z_c)}{dz}\\&=-\frac{\beta_n}{2^n}(\varepsilon_0 c n_0)^{n-1}A^{2n-1}(z,x,y,t;z_c)\\&+\ F^{-1}\left\{F\left\{i\frac{n(\omega)\omega}{c}A(z,x,y,\omega;z_c)\right\}\right\}\end{aligned} \tag{4-40}$$

differential equation was solved. Here F and F^{-1} are the Fourier- and the inverse Fourier-transformation, respectively. The first term of the differential equation describes the nth-order nonlinear absorption and the second term describes the dispersion of the crystal. The Z-scan curve, i.e., the normalized transmission T through the sample crystal, as function of the crystal position z_c can be obtained by

$$T(z_c)=\frac{\int_{-\infty}^{\infty}\int_{-\infty}^{\infty}\int_{-\infty}^{\infty}|A(z=L,x,y,t;z_c)|^2\mathrm{d}x\mathrm{d}y\mathrm{d}t}{\int_{-\infty}^{\infty}\int_{-\infty}^{\infty}\int_{-\infty}^{\infty}|A(z=0,x,y,t;z_c)|^2\mathrm{d}x\mathrm{d}y\mathrm{d}t} \tag{4-41}$$

where L is the thickness of the crystal.

It is worth noting that To filter out the closed-aperture effect at high intensities, the measured Z-scan curves have been symmetrized according to $T_s(z_c)=[T(z_c)+T(-z_c)]/2$ [104] The minima of the measured and symmetrized Z-scan curves have been fitted by varying the 3-4PA coefficient in the nonlinear pulse propagation model described before. For the fitting process, the necessary Parameters that are given to the code are the peak intensity, wavelength, Rayleigh range, phase and group refractive indices, crystal length as well as pulse length. The code also requires an initial value of the MPA coefficients. In each case, a few measured data points with the lowest

transmission values were considered for fitting by the least-square method. However, the code allows for the adjustment of another parameter, including the number of points considered around the minimum in the calculation. By default, this number was set to 5. However, trial runs were conducted with alternative settings, such as one measurement with 9 points and another with 33 points. These adjustments notably increased the time required for evaluation, particularly in the latter case. Additionally, the reliability of the results decreased, as the calculated minimum often differed significantly from the measured minimum. It's essential to note that both the Z-scan technique and the code rely on the minimum transmittance. Therefore, we contend that adding more points to the calculation may be unnecessary and could potentially introduce errors.

Chapter Five: Motivation of the work and objectives

LN crystals have large effective nonlinear coefficients which are advantageous for the generation of THz pulses by optical rectification. LT, which belongs to the symmetry class and has ferroelectric properties, is also a noteworthy material for generating THz radiation. However, there exist difficulties in increasing the scale of THz pulse energies and field strengths, such as the free-carrier absorption in the THz range induced by the multiphoton absorption of the pump. The experimental work carried out during this thesis was based on the research lines being conducted at two laboratories: the High-Field Terahertz (THz) Laboratory at the Institute of Physics, Szentágothai Research Centre, and at the Ultrafast High-Intensity Light-Matter Interactions Laboratory at the Institute for Solid State Physics and Optics, Wigner Research Centre. In accordance with them, the general objective consisting of proposing and implementing feasible solutions to the challenges involved in the precise processing of materials with two different laser sources was set out.

More specifically, the following main objectives were proposed:

1. Determination of 3PA coefficients in LN crystals.

    - We planned to use the open aperture Z-scan technique which consisted of a Ti: sapphire laser (Newport-Spectra Physics) producing 40 fs long pulses at 800 nm and 1 kHz of repetition rate in congruent (cLN) and stoichiometric (sLN) LN crystals at different Mg-doping concentrations using extraordinary polarization. The peak intensity inside the crystals varied between approximately 110 and 550 GW/cm^2.

2. Determination of 3PA coefficients in LT crystals.

    - We planned to use the same laser parameters with a similar process in undoped congruent, undoped, and Mg-doped stoichiometric LT crystals (cLT, sLT) using both ordinary and extraordinary polarized light. The peak intensity inside the crystals varied between approximately 120 and 480 GW/cm^2.

3. Determination of 4PA coefficients in LN crystals.

    - We planned to use the open aperture Z-scan technique which consisted of a Yb laser (Pharos, Light Conversion) producing 190 fs long pulses at 1030 nm at 1 kHz repetition rate in LN congruent (cLN) and stoichiometric (sLN) crystals at different Mg-doping concentrations using both ordinary and

extraordinary polarization. The peak intensity inside the crystals was 180 GW/cm^2.

4. Identify the optimum crystal composition for efficient THz generation and other nonlinear optical processes requiring high pump intensities:

   - Comparison between the 3PA coefficients in LN and LT crystals, using the same pump source at 800 nm, and a 40 fs pulse duration. This examination focused on extraordinary polarization, assuming nearly identical intensity levels: LT at I=240 GW/cm^2 and LN at I=255 GW/cm^2.

Chapter Six: Materials and Methods

6.1 Experimental setups

6.1.1 Z-scan setup for 800 nm laser

The standard open aperture z-scan setup has been carried out to measure the 3PA coefficients of LN and LT crystals, as it is illustrated in Figure 6-1. The experimental configuration comprised several critical components to ensure precise measurements. A high-performance Ti:Sapphire laser system, specifically the Newport-Spectra Physics model, was utilized. This laser source delivered ultra-short pulses with a duration of 40 fs at a central wavelength of 800 nm and 1 kHz of repetition rate. To fine-tune the power of the laser beam before it reached the sample, a combination of a half-wave plate and a linear polarizer was inserted into the setup. Focusing the laser beam onto the crystals was achieved using a lens with a focal length of 500 mm. The crystal itself was mounted on a motorized linear stage, enabling precise movement along the beam propagation direction, which is typically referred to as the z-axis. This mobility was crucial for scanning the crystal through the focal plane, an essential aspect of the Z-scan technique. A lens having a focal length of 150 mm and a diameter of 25 mm was positioned between the sample and the photodiode. This placement served the purpose of avoiding closed-aperture effects in the z-scan measurements, ND10A reflective filter was used to attenuate the beam and regulate the pump intensity. Depending on the experimental requirements, we employed a simple program written in MATLAB to both record the output and manage the translation stage responsible for moving the sample. In the case of LN crystal, a large-area Si optical power sensor with a diameter of 9.5 mm (Thorlabs S120C/PM100) was used. To perform Z-scan measurements in LT, a lock-in amplifier became essential which was synchronized with the laser's output as its trigger source. Subsequently, the amplified signal was directed into an analog-to-digital converter, and the converter's output was linked to a computer for further analysis. Si photodetector with an active area of 75 mm^2 (Thorlabs DET100A2) was used to measure the optical power of the transmitted laser beam through the LT samples.

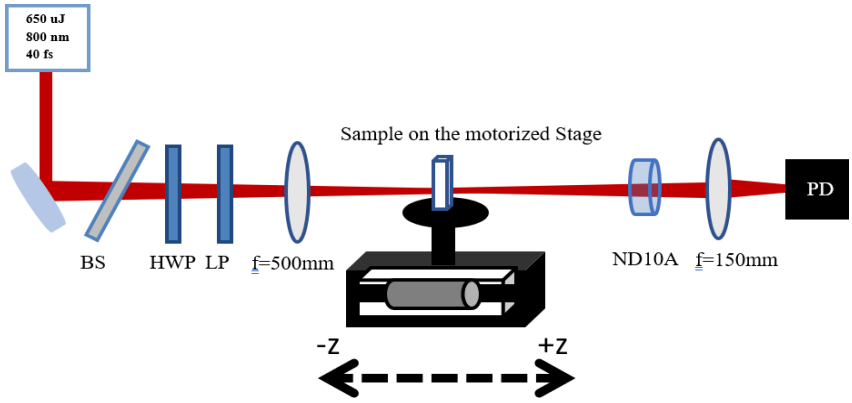

Figure 6-1: Schematic of the z-scan experimental setup. HWP: half-wave plate, LP: linear polarizer, PD: photodiode, ND10A: neutral density filter, +z shows the positive direction toward the detector, -z shows the negative direction toward the focusing lens[121].

6.1.2 Z-scan setup for 1030 nm laser

For measuring the 4PA coefficients of LN, the open aperture Z-scan setup has been carried out. As it is illustrated in Figure 6-2. the experimental setup consisted of Yb laser (Pharos, Light Conversion) producing 190 fs long pulses at 1030 nm and 1 kHz of repetitions rate, a combination of a halfwave plate and a thin film polarizer for fine adjustment of the power of the laser beam at the sample, and a lens with 400 mm focal length for focusing. The investigated LN crystal was mounted on a motorized linear stage to move it along the beam propagation direction (z-axis) around the focal plane. A lens with 150 mm focal length was used after the focal plane to eliminate the divergence of the laser beam. A large-area Si photodetector (Thorlabs DET100A2, 75 mm^2) was used for measuring the energy of the transmitted laser beam through the LN sample.

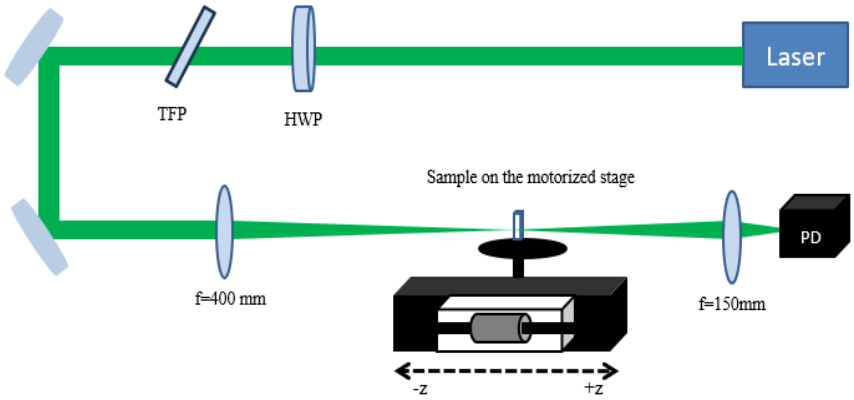

Figure 6-2: Schematic of the z-scan experimental setup. HWP: half-wave plate, TFP: thin film polarizer, PD: photodiode, +z shows the positive direction toward the detector, -z shows the negative direction toward the focusing lens [115].

6.2 Beam radius measurements

To extract an accurate multi-photon absorption coefficient from a Z-scan curve many parameters concerning the laser radiation must first be precisely determined such as radiation wavelength, repetition rate, pulse energy, and laser beam diameter. However, determining some other important parameters such as laser beam quality factor, laser beam waist radius, and Raleigh range is a must. These parameters help us get a more comprehensive knowledge of the laser's characteristics. To measure the beam radius in the horizontal direction, the knife edge was placed perpendicular to the beam and moved horizontally across the beam's path. The transmitted power data was recorded and plotted against the knife-edge position. However, the transmitted power was at 50% of its maximum value and was determined using interpolation between adjacent data points, which has been carefully measured at several positions along the propagation (z) direction. To measure the beam radius in the vertical direction, the knife edge was rotated 90 degrees so that it was perpendicular to the beam in the vertical direction with the same procedure. Having calculated the beam radius at a series of points around the focus, the sizes determined in this way are plotted in Figure 6-3 at 800 nm (left column) and 1030 (right column) wavelengths for both horizontal and vertical directions. The measurement results were fitted according to *Eq*. (4-19) This fitting allows for the calculation of the spot size (w_0), the M^2 parameter, as well as the position of the focus (z_0), and the $z_R = \pi w_0^2 / M^2 \lambda$ Rayleigh range for both horizontal and vertical directions. From the z_R's belonging to the horizontal and vertical directions a single z_R was associated with the laser beam according to $z_R = \sqrt{z_{RH} \cdot z_{RV}}$. The beam parameters determined in this way are indicated in Table 6-1 and Table 6-2 for 800 nm and 1030 nm wavelengths, respectively. These parameters were used in the simulation of the Z-scan curves. Observing the 800 nm beam reveals that its horizontal and vertical dimensions are closely aligned, within a 10% margin of each other, and the M^2 value is nearly 1.0. However, for the 1030 nm beam, the disparities are approximately twice as pronounced. Since a detailed investigation indicated a slight dependence of the obtained fitting parameters on the z range of the fittings, the fittings were repeated for a narrower z range corresponding to about $\pm 3z_R$. In Figure 6-3(b) a small difference in the position of the focal plane can be seen for the horizontal and vertical scans. Figure 6-3(a) shows a similar but smaller effect. For both cases, we applied an appropriate (0.5 mm for 800 nm beam and 1 mm for 1030 nm beam) relative shift of the “horizontal” and “vertical”

curves to achieve the same position of the beam waists. The curves obtained in this way are indicated in Figure 6-3(c) and 6-3(d). We estimated the effect of neglecting the slightly different positions of the horizontal and vertical beam-waist as follows: $1/(w_H(z) \times w_V(z))$ was calculated with the original fitting curves and with the modified ones. The results are shown in Figures 6-3(e) and 6-3(f). In Figure 6-3(e) the two curves are indistinguishable, in Figure 6-3(f) the difference between the maxima of the two curves is less than 1%. So we can neglect the effect of the shift of the curves on the beam intensity function.

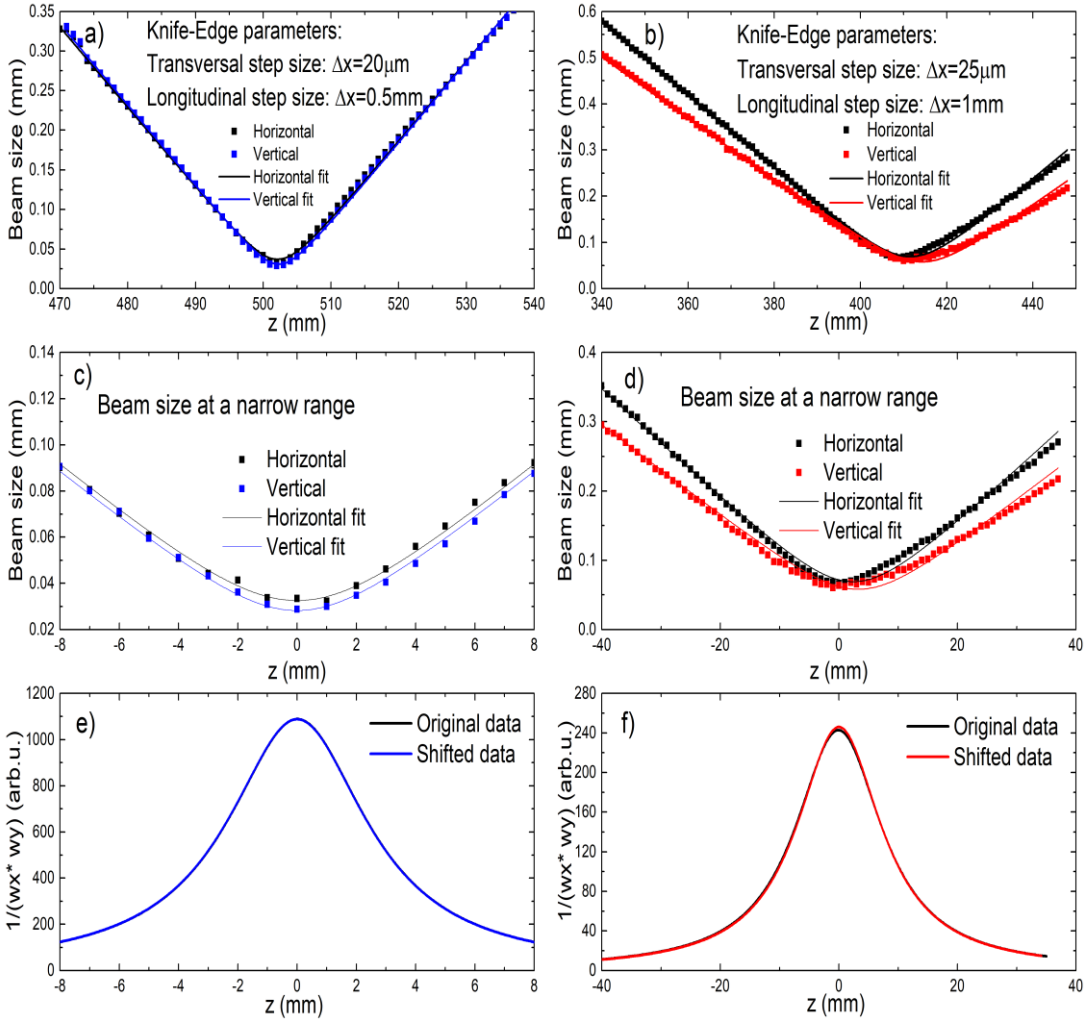

Figure 6-3: The measured horizontal and vertical spot sizes versus the propagation coordinate for 0.8 μm and 1.03 μm (a,b). The same is indicated for an about $\pm 3z/z_R$ range (b,c). Relative intensity curves are calculated with the original and the shifted data (e,f) [115].

Table 6-1: Beam parameters of the 0.8 μm beam determined by the knife-edge method.

		spot size w_0 (μm)	M^2 parameter	Rayleigh range (mm)
Broad range	Horizontal	36	1.48	3.61
	Vertical	30	1.23	2.96
Narrow range	Horizontal	32	1.36	3.03
	Vertical	28	1.16	2.68

Table 6-2: Beam parameters of the 1.03 μm beam determined by the knife-edge method.

		spot size w_0 (μm)	M^2 parameter	Rayleigh range (mm)
Broad range	Horizontal	69	1.69	8.65
	Vertical	57	1.18	8.64
Narrow range	Horizontal	69	1.60	8.66
	Vertical	56	1.16	8.60

6.2 Sample preparation

The samples were examined in the experiment to determine 3PA and 4PA coefficients by applying the Z-scan technique, as detailed in Table 6-3. Both LN and LT crystals were chosen at different Mg doping concentrations. For LN crystals, the measurements were carried out at 110, 255, 290, and 555 GW/cm² pump intensity for extraordinary polarization at 800 nm, and the measurements were performed at 180 GW/cm^2 pump intensity (inside the sample) for both ordinary and extraordinary polarization at 1030 nm. These variations in pump intensity enabled us to study the absorption coefficients that respond to different energy inputs. In the case of LT crystals, measurements were conducted at 120, 240, 360, and 480 GW/cm² pump intensities for both ordinary and extraordinary polarization at 800 nm wavelength. This comprehensive approach allowed for a detailed analysis of the crystals' behavior under varying pump intensities, considering the effects of both ordinary and extraordinary polarization. The samples were scanned in the vicinity of the lens focus ($z = 0$) starting from a position ahead of the focus (negative z) and moving toward a position behind the focus (positive z). Table 6-3 summarizes the properties of the studied crystals:

Table 6-3: Parameters of the studied samples

Crystal	Notation of sample	Mg doping level (mol%)	Size (x,z) (mm)	Thickness (mm)
$LiNbO_3$	sLN:4.18% Mg	4.18	7×8	0.610
	sLN:1.50% Mg	1.50	3×6	0.600
	sLN:0.67% Mg	0.67	4.15×5	0.605
	cLN	0.0	5×10	0.600
	cLN:1.0% Mg	1.0	5×6	0.601
	cLN:6.0% Mg	6.0	12×6	0.600
$LiTaO_3$	sLT	0.0	10×5	0.520
	sLT:0.5% Mg	0.5	10×5	0.519
	sLT:1.0% Mg	1.0	11.3×10.3	0.514
	cLT	0.0	11×10	0.176

6.4 UV absorption spectra

The absorption characteristics of the LN samples under investigation were measured at different concentrations of Mg-doping around the UV absorption edge. The results were analyzed for both ordinary (left column) and extraordinary (right column) polarizations. It is important to note that the detector reached saturation at an absorbance value exceeding 3, equivalent to an absorption coefficient of about 120 cm^{-1}. In the graphical representation, wavelengths three times smaller than 800 nm were indicated by a green dashed line on the left, and those at 1030 nm were indicated by a green dashed line on the right. Notably, at the 800 nm wavelength, the three-photon energy falls within the saturated region. This implies that it is sufficient to excite the valence electrons to the conduction band. However, this is not the case for the 1030 nm wavelength. Consequently, it can be asserted with certainty that the dominant effect at 800 nm is the three-photon absorption (3PA), whereas at 1030 nm, is the four-photon absorption (4PA).

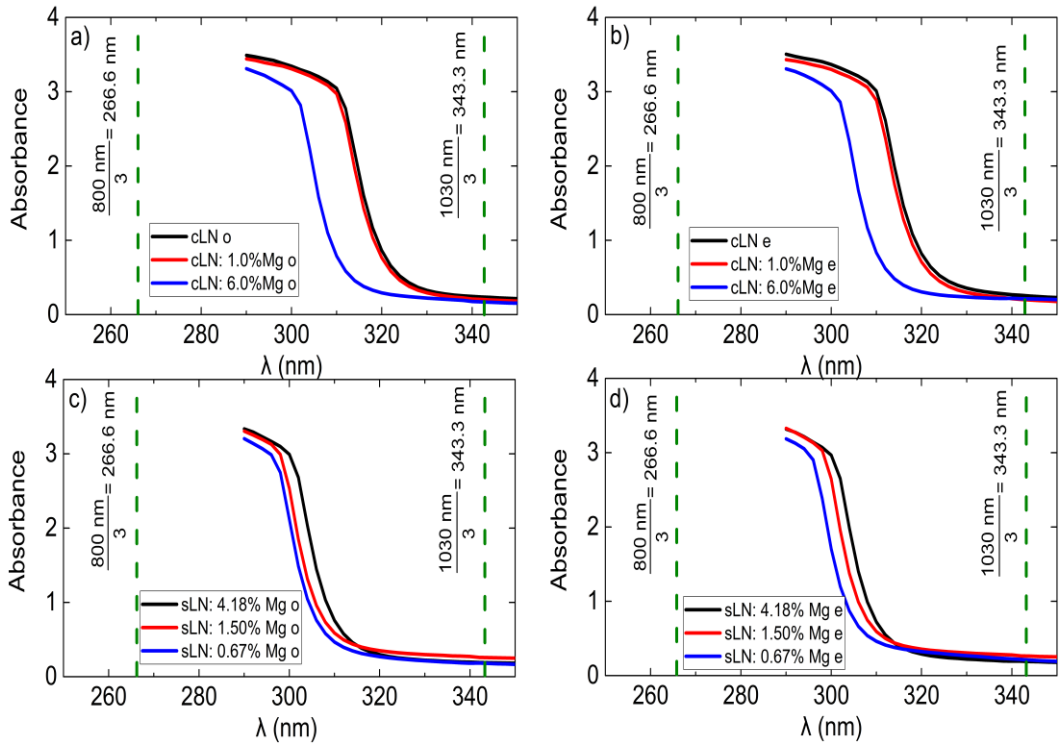

Figure 6-4: UV absorption spectra for all the investigated lithium niobate crystals for both ordinary and extraordinary polarized light [115].

In Figure 6-5, the absorbance spectra for all LT crystals are depicted, showcasing measurements in the UV range under both ordinary (Figure 6-5a) and extraordinary (Figure 6-5b) polarization. The saturation observed above 2.5 corresponds to the device's operational limit. While acknowledging that the placement of samples in the spectrometer introduces a minor uncertainty in the absolute absorbance value, the pivotal outcome lies in identifying the wavelength at which absorbance sharply rises. This observed phenomenon is considered reliable and is consistent with findings from other references [103], particularly concerning discerning differences between congruent and stoichiometric compositions and establishing the position of the UV absorption edge for stoichiometric and congruent compositions. In the upcoming discussion, a comprehensive evaluation of the significance of these findings will be conducted.

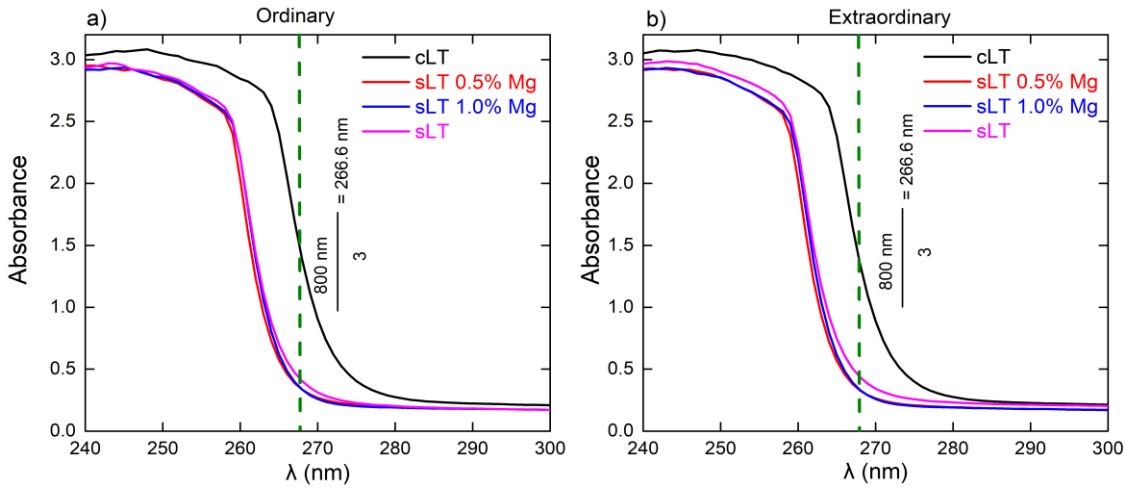

Figure 6-5: UV absorption spectra for all the investigated lithium tantalate crystals for both ordinary and extraordinary polarized light.

For the determination of the MPA coefficients, the application of the open aperture Z-scan measurement was intended. However, the measured Z-scan curves show slight asymmetry (see Figure 6-6a), an effect attributed temporarily to self-focusing caused by nonlinear refraction, or photo-refraction, indicating that the detector was not large enough. Because of this we separated the effect of MPA and self-focusing by applying the subtraction method described in section 4.1.1. In this way, we obtained symmetric curves as it is indicated in Figure 6-6b.

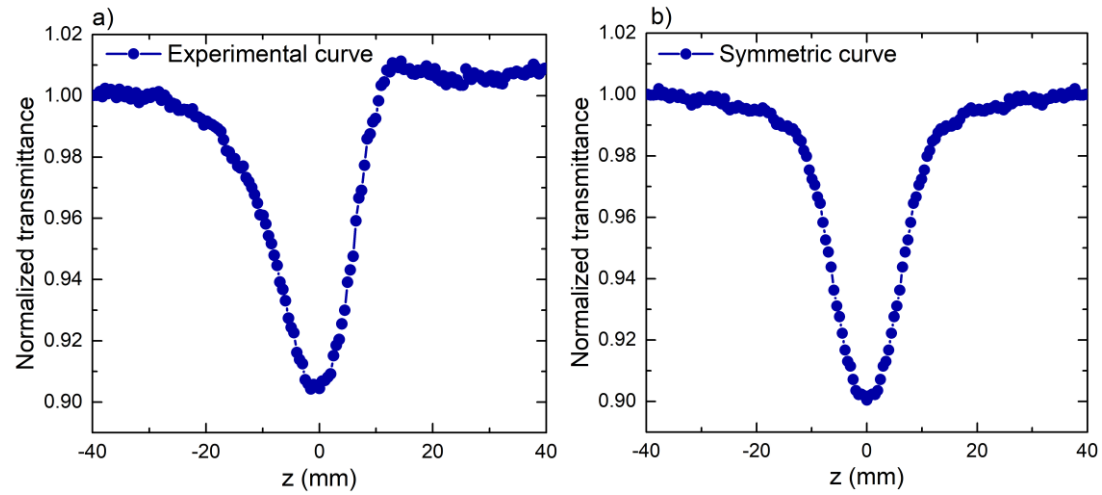

Figure 6-6: As an example, the directly measured z-scan curve (a), measured with 1.03 μm beam, and the symmetrized curve (b) is shown in the case of sLN:1.50% Mg crystal for ordinary polarization [115].

Chapter Seven: Results

7.1 Z-scan curves obtained for 800 nm laser

7.1.1 Lithium niobate

In this study, laser measurements were performed at a wavelength of 800 nm, specifically in the extraordinary polarized light. The minima of these modified z-scan curves have been fitted by varying the 3PA coefficients in our nonlinear pulse propagation model as described in section 4.4.1. (Since LN has a band-gap of about 3.8 eV, the maximum wavelength where 3PA possible is $\lambda_{3PA} = \frac{3hc}{E_g} = 980\ nm.$) In each case, five measured data points with the lowest transmission values were considered for fitting by the least-square method, and the MPA coefficient was the only fitting parameter. The resulting data, along with fitted curves, are presented in Figure 7-1, organized into two columns representing different crystal samples: cLN on the left and sLN on the right. These samples vary in magnesium (Mg) doping concentration, with the graphs ordered in both columns based on the crystal's defect concentration. The top row displays samples with the highest defect concentrations, while the bottom row features samples with the lowest defect concentrations. The intensity values indicated on the graphs represent the peak intensity at the center of the laser beam within the samples. Remarkably, most of the experimental data points (represented as dots) match well with the fitted curves, except for the samples with the lowest intensity, specifically the sLN:4.18% Mg and cLN:1.0% Mg samples. According to the indicated 3PA coefficients resulting in the best fit, the 3PA coefficients exhibit a maximum value at the intensity of about 290 GW/cm² across all the crystal compositions investigated.

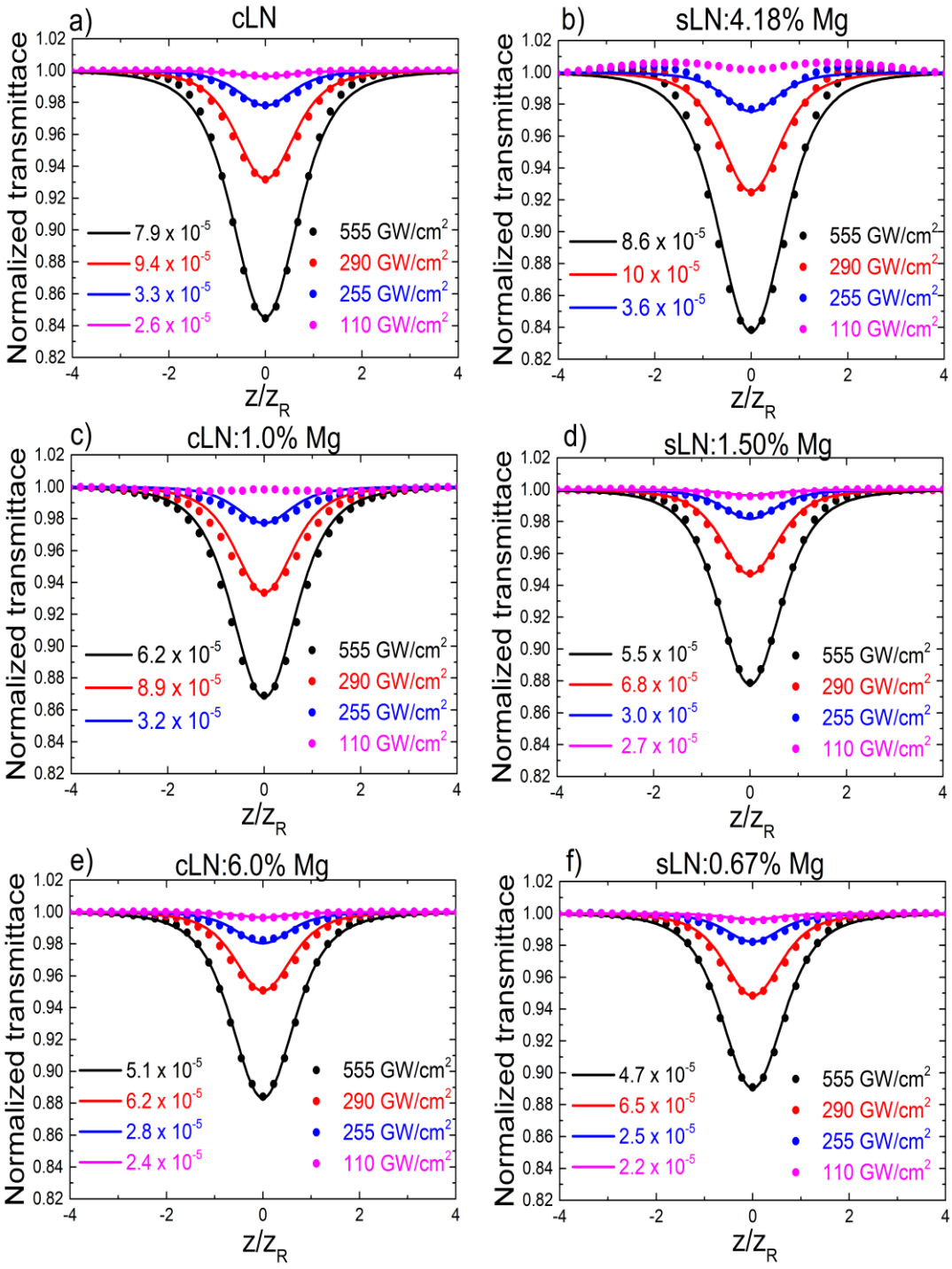

Figure 7-1: Result of z-scan measurements (dots) together with fitting curves for different crystals and laser intensities. The 3PA coefficients resulting the best fitting are indicated. β_3 is measured in cm^3/GW^2[115].

Figure 7-2a and b present the measurement and fitting results obtained at an intensity of 290 GW/cm^2 for sLN and cLN crystals, respectively. These results highlight the interesting relationship between the composition of these crystals and the three-photon absorption coefficient (3PA). One of the key takeaways from these figures is the

observation of a relatively small composition dependence in both sLN and cLN crystals but the 3PA coefficient is smallest for compositions with specific Mg doping concentrations. For sLN, this minimum is achieved at sLN:0.67% Mg, while for cLN, at cLN:6.0% Mg. These specific concentrations are of particular interest because they closely approach the photorefraction suppression threshold [35,105].

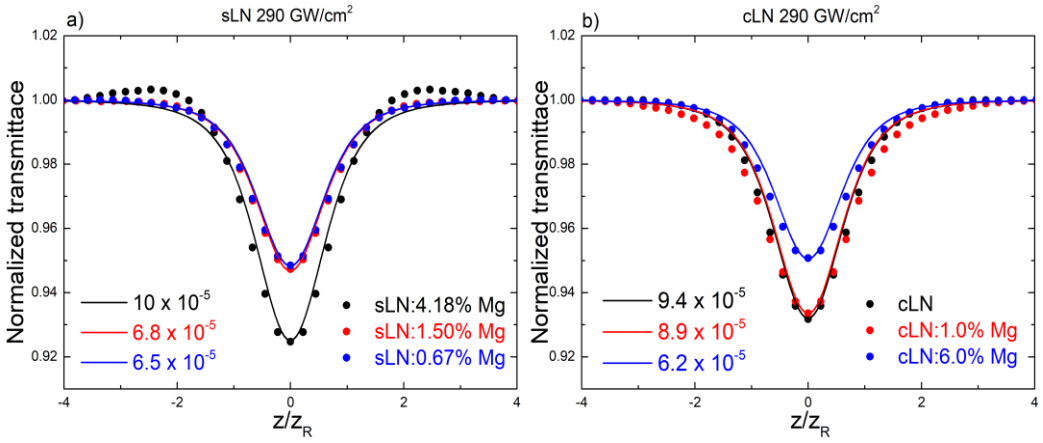

Figure 7-2: Result of the z-scan measurements (dots) together with fitting curves for sLN (a) and cLN (b) at 290 GW/cm^2 for different crystal compositions. β_3 is measured in cm^3/GW^2 [115].

In Figure 7-2(a), a 0.5% increase in the measured transmission can be observed, followed by the valley corresponding to 3PA. The possible reason for this increment could be due to the linear absorption of some contamination on the sample during the growth, or it could be related to the saturation of a transition state caused by pumping, or even more complex processes could be behind it. In the case of the Z-scan measurement of malachite crystal, various nonlinear mechanisms were necessary to be considered in the fitting model for this reason [106]. In Table 7-1, all the calculated coefficients for 3PA coefficients in LN are listed.

Table 7-1: Three-photon absorption coefficients of all LN samples for extraordinary polarization

	β_3 ($\times 10^{-5}$ cm^3/GW^2) 800 nm			
	110 GW/cm^2	255 GW/cm^2	290 GW/cm^2	555 GW/cm^2
sLN: 4.18% Mg	-	3.6	10	8.6
sLN: 1.50% Mg	2.7	3.0	6.8	5.5
sLN: 0.67% Mg	2.2	2.5	6.5	4.7
cLN	2.6	3.3	9.4	7.9
cLN: 1.0% Mg	-	3.2	8.9	6.2
cLN: 6.0% Mg	2.4	2.8	6.2	5.1

In Figure 7-3, the normalized 3PA coefficients are depicted versus varying doping concentrations for different intensities, with the corresponding error bars. To improve trend clarity, I have normalized the values, aligning their minima with or close to the Mg doping levels that correspond to the thresholds for suppressing photo-refraction at specific concentrations—0.67% Mg for sLN and 6% Mg for cLN. Determining intensity with higher accuracy poses challenges. If we assume a 5% margin of error in these measurements, it suggests that the overall error could be around 15-20%. However, the initial estimation of 50% may have been overestimated. In light of these, a thorough assessment using error propagation calculations becomes important. By assuming the relative errors (5% Horizontal beam radius, 5% Vertical beam radius, 5% pulse duration, and 1% from Energy) the error of the intensity I obtained was 8.7% which is significant, multiplied by n-1, which suggests that the error could be 17.4%. However, it is not clear in the works of literature that the calculation of MPA whether the intensity used inside the crystal or outside the crystal.

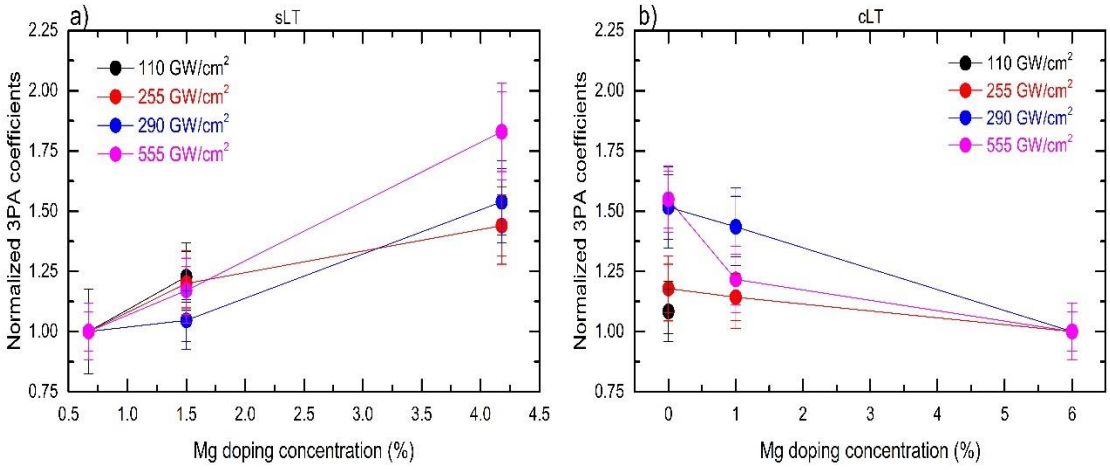

Figure 7-3: Normalized 3PA coefficients versus different Mg doping concentrations at different pump intensities with the corresponding error bars.

7.1.2 Lithium tantalate

Conditions of multi-photon absorption are intrinsically linked to the band gap energy of the crystals. Considering the E_g = 4.9 eV optical band gap of LT [57] mentioned earlier, the expected border wavelength between 3PA and 4PA ranges would be at $\lambda_p = 3hc/E_g$ = 761 nm, where h is the Planck constant and c is the speed of light. However, it seems that in Ref. [57], the value of E_g was overestimated. They measured UV

absorption in the wavelength range longer than 270 nm and considered the photon energy corresponding to α = 10,000 cm^{-1} as E_g by extrapolation. However, in a recent paper where the bandgap of LN was obtained by a well-established method, accepted in solid-state physics, it was found that the linear absorption of the sample was 25 cm^{-1} at the wavelength corresponding to the measured bandgap [34]. Although the paper is about LN, however, the similarities with LT allow for a conclusion that based on the strict analysis proposed in the article, we anticipate the bandgap energy to be at a substantially lower absorption value of $\alpha = 25$ cm^{-1}. According to the curves shown in Figure 6-5, at congruent composition, this α = 25 cm^{-1} absorption coefficient can be converted to absorbance which is above/around 275 nm indicating the effect of 3PA clearly. For the other composition, the proposed absorption level is on the border, hence another method is necessary to further clarify the prevailing absorption order. To ascertain through an alternative approach whether 3PA or 4PA is the dominant MPA process at 800 nm, we first performed a Z-scan measurement with an sLT:0.5% Mg crystal, which has the highest E_g according to Figure 6-5. We examined whether the measured curve could be better fitted with the curve calculated under the assumption of 3PA or 4PA. Figures 7-4a and b show the measurement and fitting results at 360 GW/cm^2 intensity for ordinary and extraordinary polarizations, respectively. The fitting curves supposing 4PA are significantly narrower than the measured ones for both ordinary and extraordinary polarisations. However, the fitting curves supposing 3PA show good agreement with the measured ones for both polarizations. So, we can conclude that in the case of sLT:0.5% Mg crystal 3PA is the dominant MPA effect. Since according to Figure 6-5 the other crystals have the same or even smaller band gap, in the following we use fitting curves supposing 3PA for all LT crystals.

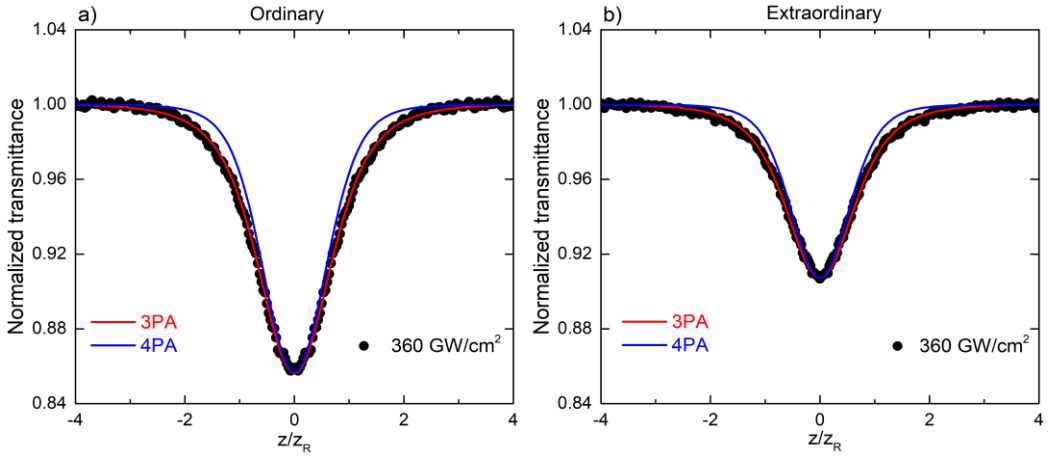

Figure 7-4: As an example, the result of the z-scan measurements (dots) together with fitting curves of

3PA (red line) and 4PA (blue line) for sLT:0.5% Mg crystal, ordinary (a) and extraordinary (b) polarization at 360 GW/cm^2 [121].

For all investigated crystals and applied laser intensity, the measured results after symmetrization and normalization, together with the fitting curves supposing 3PA are plotted in Figure 7-5 both for the ordinary (left column) and extraordinary (right column) polarization. For each curve, the given intensity values correspond to the peak intensities I_0 at the beam centre inside the sample. The measured data points are close to the fitting curves for every intensity except the lowest one at which the noise becomes significant. Both for cLT and sLT crystals, the transmission curves are significantly deeper for ordinary polarization than for extraordinary polarization. Accordingly, the calculated 3PA coefficients, indicated in Table 7-2 and plotted in Figure 7-5, are larger for ordinary polarization than for extraordinary polarization.

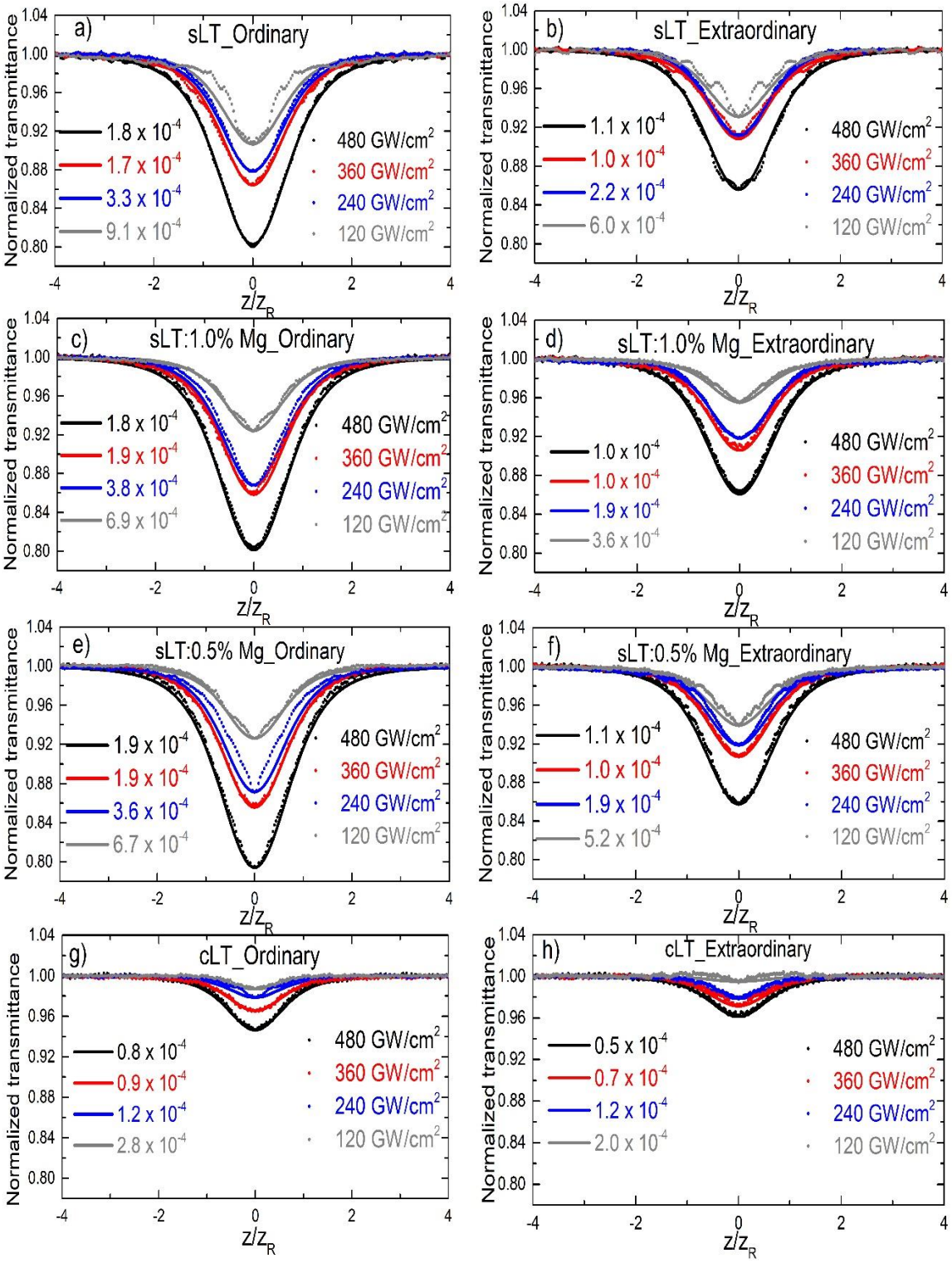

Figure 7-5: Result of z-scan measurements (dots) together with fitting curves for different LT crystals at different laser intensities. The 3PA coefficients resulting the best fitting are indicated in cm^3/GW^2 [121].

Table 7-2: Three-photon absorption coefficients in Lithium tantalate for ordinary and extraordinary polarization at 800 nm

	β_3 ($\times 10^{-4}\ cm^3/GW^2$)							
	Ordinary				Extraordinary			
Intensity (GW/cm^2)	480	360	240	120	480	360	240	120
cLT	0.8	0.9	1.2	2.8	0.5	0.7	1.2	2.0
sLT	1.8	1.7	3.3	9.1	1.1	1.0	2.2	6.0
sLT:0.5% Mg	1.9	1.9	3.6	6.7	1.1	1.0	1.9	5.2
sLT:1.0% Mg	1.8	1.9	3.8	6.9	1.0	1.0	1.9	3.6

7.2 Z-scan curves obtained for 1030 nm laser

7.2.1 Lithium niobate

With 1030 nm laser measurements were employed at only one pump intensity (180 GW/cm^2), but both ordinary and extraordinary polarizations were performed. The measured results after symmetrization and normalization, together with the fitting curves are plotted in Figure 7-6 both for the cLN (left column) and sLN (right column) samples with different Mg-doping concentrations. The results for the extraordinary polarization are indicated in the first row, and for the ordinary one in the second row, respectively. Upon initial observation, it is readily apparent that the Z-scan curves obtained from measurements exhibit a notable disparity when compared to the fitting curve based on the assumption of a four-photon absorption (4PA) model. This contrasts with the situation observed at a wavelength of 0.8 μm. In a majority of instances, the width of the measured curves is considerably larger than that predicted by the theoretical fitting curves. Furthermore, inspecting the Z-scan curves measured at extraordinary polarization, it is very surprising that, contrary to the fact that at 1.03 μm only 4PA is possible, while at 0.8 μm the usually stronger 3PA is the lowest order MPA, the absorption for 1.03 μm at 180 GW/cm^2 is between the absorptions obtained for 0.8 μm at 110 and 255 GW/cm^2, respectively (see Figure 7-5), adding to that was observed with the sLN:4.18% Mg crystal, which displayed significantly higher absorption at 1.03 μm compared to 0.8 μm. In cases where the defect concentration reaches its maximum, such as in sLN with 4.18% Mg, and cLN (ordinary polarization), the observed transmission valleys are characterized by widths that exceed the confines of the fitting

window. Consequently, attempts at fitting these curves yield suboptimal results. Given that these specific materials, (sLN with 4.18% Mg) and (cLN without doping), demonstrate impractical levels of THz absorption and unusably high photorefraction, as outlined in previous research [107], the measured transmission characteristics in these high-defect-concentration cases are challenging to reconcile with the fitting window, and the resulting fits do not offer practical insights due to the unfavorable physical properties associated with these materials. As a result, they have been left out of the evaluation process. Similar to the 0.8 μm case, at 1.03 μm, the absorption had a minimum value at a specific magnesium doping concentration that corresponds to a threshold where photorefraction is suppressed. However, for 1.03 μm the magnesium doping dependence is much stronger than for 0.8 μm. The Z-scan curves obtained under extraordinary polarization showed more scattering at 1.03 μm compared to 0.8 μm, and in most cases, the measured curve widths were significantly larger than the theoretical fitting curves. Additionally, the Z-scan curves measured under ordinary polarization indicated significantly higher absorption compared to those measured under extraordinary polarization. This difference was particularly pronounced for crystals like cLN and sLN:4.18% Mg, which had magnesium doping concentrations far from the photorefraction suppression threshold. These findings suggest that at 1.03 μm, the predominant cause of nonlinear absorption is not genuine four-photon absorption (4PA). However, we have derived 'effective' 4PA values through a fitting process, offering a useful basis for designing nonlinear optical applications under the specific intensities employed in our measurements. An essential point to consider, is that ordinary polarization indicates significantly larger absorption than the ones measured for extraordinary polarization. It can be realized that the fit is poor and not able to determine the 4PA in the case of sLN:4.18% Mg and cLN, but since the doping level is not practical for the applications due to the corresponding high THz absorption or high photorefraction (sLN:4.18%Mg and cLN, respectively) [107].

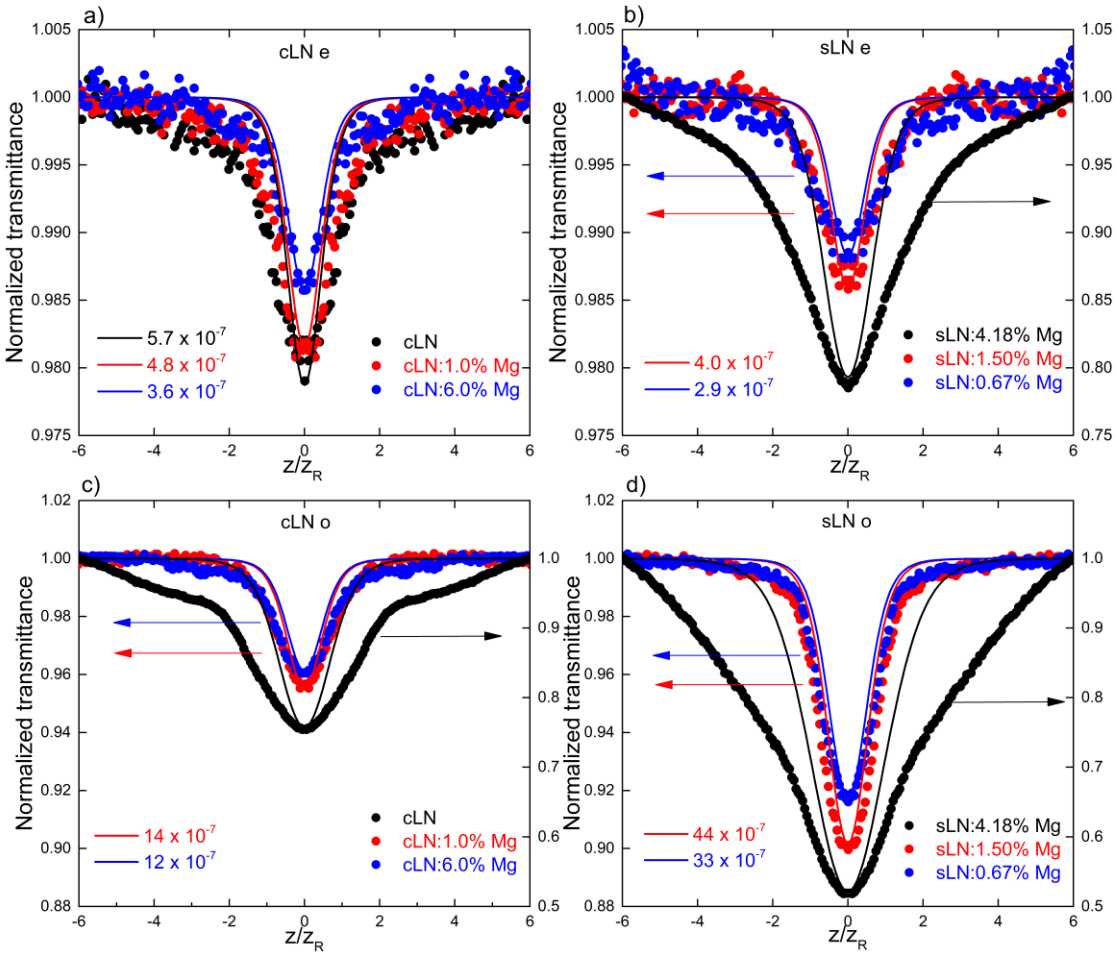

Figure 7-6: Result of the z-scan measurements (dots) together with fitting curves for cLN (a, c) and sLN (b, d) crystals with different Mg doping levels at 180 GW/cm^2 laser intensity for extraordinary (a,b) and ordinary (c,d) polarization. β_4 is measured in cm^5/GW^3 [115].

Table 7-3: Four-photon effective absorption coefficients of all samples for ordinary and extraordinary polarization at 1030 nm

	β_4 ($\times 10^{-7}$ cm^5/GW^3)	
	Ordinary	Extraordinary
	180 GW/cm^2	
sLN: 4.18% Mg	-	-
sLN: 1.50% Mg	44	4.0
sLN: 0.67% Mg	33	2.9
cLN	-	5.7
cLN: 1.0% Mg	14	4.8
cLN: 6.0% Mg	12	3.6

Chapter Eight: Discussion

Initially, it is essential to consider several aspects regarding the accuracy of MPA coefficient measurements. The determination of MPA coefficients is based on measuring the relative change in transmission. As clearly illustrated in Figures 7-1, 7-5, and 7-6, we can achieve a remarkable accuracy level using techniques such as lock-in amplifier or other forms of averaging, with measurements better than 1%. This approach ensures that the fluctuations in the signal are effectively minimized, resulting in highly precise measurements of relative changes in transmission. However, the calculated MPA coefficient depends on the absolute value of the intensity too and the determination of the intensity is possible only with much less accuracy. The reason is that the determination of the intensity is usually based on *Eq*. (4-38). This equation provides an exact description of intensity for beams with perfectly Gaussian temporal and spatial distributions. Moreover, measuring the pulse duration and beam waists with superior precision is a challenging task, often limited to an accuracy of no better than 5%. When these limitations are taken into account and considering the error propagation inherent in the measurement process, we typically encounter an accuracy range for intensity determination of ±15% to ±20% this range reflects the potential variability in the accuracy of the intensity measurement of which the intensity values vary between ±15% at its best and ±20% at its worst. This variation in intensity determination translates to a proportional increase in uncertainty in the determination of n^{th}-order MPA coefficients. It results in an approximately n-1 times larger margin of error in the determination of these coefficients.

8.1. Multiphoton absorption in LN

Initiate the comparison of our results with previous findings by discussing the 4PA coefficient. Reference [24] provides insights into this coefficient for LN, a material compositionally similar to our sample and subjected to identical laser polarization. In their study, a β_4 value of 3.0×10^{-6} cm^5/GW^3 was reported for Mg-doped sLN when exposed to a 1050 nm laser at an intensity of 200 GW/cm^2 with extraordinary polarization. Although the specific doping concentration isn't specified, it's reasonable to infer it was around 1%, a typical concentration for such crystals. Notably, this reported 4PA coefficient value is approximately an order of magnitude higher than our measured values for 0.7% and 1.5% Mg-doped sLN crystals, where we observed β_4

values of 2.9×10^{-7} cm^5/GW^3 and 4.0×10^{-7} cm^5/GW^3 respectively (refer to Table 7-3). The discrepancy between these values cannot be solely attributed to inaccuracies in laser intensity measurements. Rather, it's plausible that the longer pulse duration (1 ps) and significantly larger repetition rate (50 kHz) of the laser used in the measurement reported in Ref. 24 could lead to a larger 4PA coefficient. Nearly three decades prior, Henari et al. observed nonlinear absorption in cLN using a continuous-wave (cw) Ar-ion laser at 514 nm [108]. Employing the Z-scan method, they measured a substantial nonlinear absorption coefficient of $\beta = 5\times10^6$ cm/GW^2. Subsequent investigations by Pálfalvi et al., utilizing similar techniques but with LN crystals exhibiting suppressed photorefraction, yielded coefficients three orders of magnitude smaller, yet still significant. For instance, in 0.7% Mg-doped sLN, they found β values of 1.7×10^3 cm/GW^2 and 0.55×10^3 cm/GW^2 for extraordinary and ordinary polarization respectively. In these instances, given the relatively low (cw) laser intensities employed, direct two-photon absorption is unlikely to be the primary cause of the observed nonlinear absorption. Instead, two-step processes involving crystal defects probably play a pivotal role. Reference [108] suggests the appearance of polarons Nb^{4+} and O^- intrinsic defects as potential intermediate levels involved in this two-step process. In our experiments, as well as in the study cited as Reference [24], a Yb-laser operating at a wavelength of 1030 nm was employed. Due to the relatively low photon energy associated with this wavelength, neither real two-photon absorption nor two-step, intermediate-level mediated two-photon absorption are possible. However, it is important to highlight that second-harmonic generation (SHG), while non-phase matched, could potentially generate intense pulses within the examined LN crystals at a wavelength of 515 nm. This phenomenon arises from the longer l_c SHG coherence length of the ooe (ordinary + ordinary → extraordinary) SHG process, which exceeds 100 µm for certain crystal compositions (refer to Table 8-1), particularly under ordinary input polarization. To assess the significance of the 515 nm light produced through this mechanism, we conducted experiments utilizing our Z-scan setup. Specifically, we positioned the sLN:4.18% Mg crystal at the focal point of the Yb-laser pulses, which exhibited an intensity of 180 GW/cm^2. Our observations revealed SHG with an external efficiency ranging between 6% and 8%. Despite the considerably shorter coherence length for the eee process, resulting in a SHG efficiency approximately 100 times smaller for extraordinary-polarized 1030 nm wavelength, the generated 515 nm

radiation at an intensity of 100-200 MW/cm² could induce notable two-photon absorption. It is noteworthy that nonlinear absorption, as observed in previous references [105] and [108], is attributed to a two-step process involving crystal defects. This suggests that the absorption mechanism is dependent not only on the intensity of light but also on its fluence. Consequently, employing longer pulse durations and higher repetition rates may augment additional absorption via the two-step process linked to crystal defects. This phenomenon could explain the observed disparity in the measured 4PA coefficient, with Reference [24] reporting a coefficient approximately one order of magnitude larger compared to our findings. Furthermore, the increased absorption due to this additional mechanism may clarify the substantial disparity in the measured 4PA coefficient between ordinary and extraordinary polarizations (with stronger SHG), as detailed in Table 7-3. It also provides insight into why the 4PA coefficient reaches its maximum for crystal compositions (cLN and sLN:4.18% Mg) exhibiting the highest defect concentration, representing an intermediate state of the two-step absorption process. For instance, in cLN crystals, there exists approximately 1 mol% of antisite Nb ions (Nb_{Li}, Nb on Li site), alongside about 4 mol% of charge compensating Li vacancies. Similarly, in sLN:4.18% Mg crystals, a variety of extrinsic and intrinsic defects may occur on a percentage scale, such as Mg either on Li or Nb site and Li vacancies. It is noteworthy that the transition between the valence and conduction bands induced by 4PA of a 1030nm laser, along with 2PA of a 515 nm laser and SHG pulse, in the presence of crystal defects mentioned earlier, can effectively give rise to various types of polarons [109]. These polarons exhibit broad absorption bands in the visible spectrum, facilitating the two-photon absorption of the 1030 nm laser pulse. The lifetimes of these polarons allow for their accumulation at the repetition rates of 1 kHz utilized in our experiments, and even more so at the 50 kHz repetition rate employed in Reference [24]. At a wavelength of 800 nm, the SHG coherence length for extraordinary polarization is only between 1.0 and 1.5 μm, resulting in negligible SHG. Consequently, the additional absorption through the two-step process is also minimal. This could potentially contribute to the 3PA at 800 nm not exhibiting a greater strength than the 4PA at 1.03 μm wavelength. Moreover, it is important to mention that during an investigation into the intensity dependence of MPA of various orders in a chalcogenide glass possessing a bandgap energy of 2.5 eV, it was discovered that MPA of higher order surpassed the 4PA of the 3PA at intensities exceeding 30 GW/cm² [110].

Given these insights, it wouldn't be unexpected if a similar trend is observed, as suggested by our results, within the range of 100 to 200 GW/cm² for LN with a bandgap energy of 3.8 eV.

Table 8-1: Calculated coherence length (l_c) for second harmonic generation (SHG) in both oo-e and ee-e SHG processes in a few LN crystal compositions. n_o and n_e are the refractive indices for ordinary and extraordinary polarizations, respectively.

Crystal	Wavelength (μm)	n_o	n_e	Ref	Process	l_c (μm)
cLN	1.03	2.2351	2.1584	[111]	oo-e	26.54
	0.515	2.3356	2.2448		ee-e	2.98
	0.8	2.2541	2.1749		oo-e	2.78
	0.4	2.4317	2.3260		ee-e	1.32
cLN:5.0% Mg	1.03	2.2319	2.1506	[112]	oo-e	533
	0.515	2.3283	2.2324		ee-e	3.14
	0.8	2.2527	2.1683		oo-e	3.06
	0.4	2.4307	2.3180		ee-e	1.33
sLN	1.03	2.2370	2.1567	[113]	oo-e	29.59
	0.515	2.3410	2.2457		ee-e	2.89
	0.8	2.2571	2.1745		oo-e	4.40
	0.4	2.4089	2.3025		ee-e	1.56
sLN:4.5% Mg	1.03	2.2257	2.1453	[114]	oo-e	157.01
	0.515	2.3220	2.2274		ee-e	3.13
	0.8	2.2465	2.1634		oo-e	2.92
	0.4	2.4249	2.3150		ee-e	1.31
sLN:3.3% Mg	1.03	2.2292	2.1454	[114]	oo-e	136.96
	0.515	2.3260	2.2274		ee-e	3.14
	0.8	2.2509	2.1639		oo-e	3.17
	0.4	2.4330	2.3139		ee-e	1.33
sLN:2.0% Mg	1.03	2.2326	2.1451	[114]	oo-e	43.71
	0.515	2.3294	2.2267		ee-e	3.15
	0.8	2.2538	2.1636		oo-e	3.46
	0.4	2.4330	2.3116		ee-e	1.35
sLN:0.78% Mg	1.03	2.2342	2.1456	[114]	oo-e	36.16
	0.515	2.3306	2.2271		ee-e	3.15
	0.8	2.2555	2.1639		oo-e	3.36
	0.4	2.4389	2.3150		ee-e	1.32

8.2. Multiphoton absorption in LT

The graphs in Figure 8-1 indicate the intensity dependence of the 3PA coefficients for ordinary and extraordinary polarization. The 3PA coefficient of cLT is significantly (about a factor of two) smaller than that of sLT. The main finding shows that as the intensity level of the light increases, the 3PA coefficients decrease for ordinary and extraordinary polarized light in both types of lithium tantalate crystals (sLT and cLT). These observations are in agreement with supposing an additional 3PA process caused by crystal defect states generated by the Mg doping and the saturation of this process at high intensity.

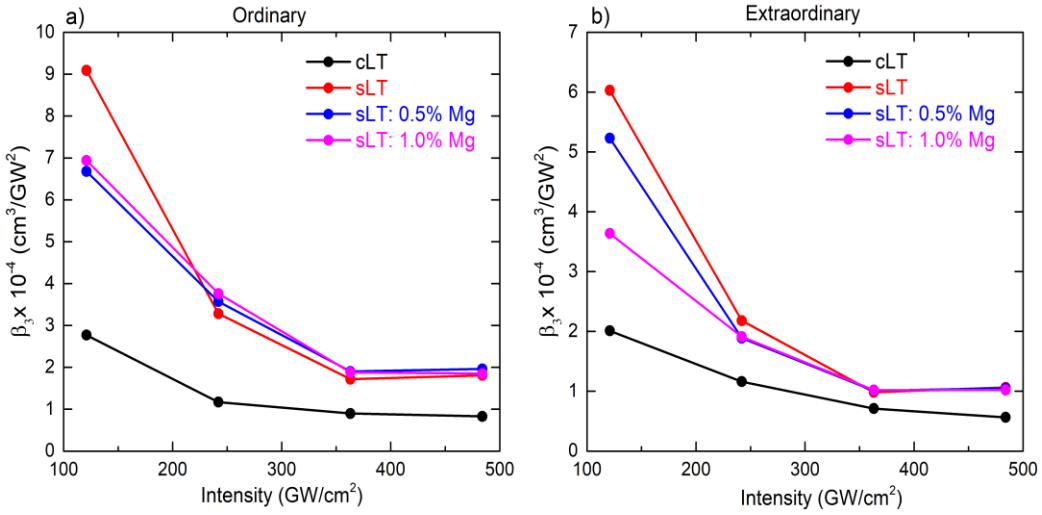

Figure 8-1 Three-photon absorption coefficients of cLT and sLT crystals versus the pumping intensities for ordinary (a) and extraordinary (b) polarization [121].

It should be pointed out, however, that, at light intensities above the saturation value, the photon absorption coefficient decreases. This type of saturation was observed for 2PA in [26]. With higher intensity, MPA decreases, which is true for both 2PA and 3PA. Our determined I_{sat} (see Figure 8-2) for 3PA appears to be similar to the I_{sat} for 2PA in Ref. 26. Regarding the determination of saturation intensity for 3PA, we got the idea from the work of [26] although their study primarily focused on 2PA. While their findings hinted at the presence of saturation, they did not delve into the underlying physical processes causing it. While doping does not appear to be a significant factor influencing saturation. A hyperbolic approximation is used to model the intensity dependence of 2PA coefficient β.

$$\beta(I) = \beta_0/(1 + I/I_{sat}) \qquad (8\text{-}1)$$

where β_0 is the 2PA coefficient at low pulse intensity, I_{sat} is the pulse intensity which induces the 2PA coefficient decrease. They determined a saturation intensity of 11 GW/cm^2. For our case where 3PA is present, we made the same type of calculations we achieved a relatively good fitting if we suppose the same saturation intensity of 11 GW/cm^2. However, we note that the fitting is not very sensitive for the exact value of I_{sat} in a factor of two does not change too much. Similarly, we agree with the finding that the MPA is smaller in the case of a congruent crystal. The polarization-dependent behaviour could be attributed to the crystal's anisotropic properties. However, it is not plausible that the different efficiency of second harmonic generation (SHG) for the two laser polarizations, and a subsequent low-order absorption are responsible for this behaviour, as was supposed in Ref. [115] for lithium niobate pumped at 1.03 μm. Namely, for LT and 800 nm, the coherence length of the SHG process is only about 1.5 μm (see table 8-2), and the same for the two polarizations. The significantly smaller 3PA coefficient of cLT than that of sLT could be due to the quantities of intrinsic defects being different. The different stoichiometry in the crystal structure can cause variations in the way photons interact with the crystal, leading to differences in absorption coefficients.

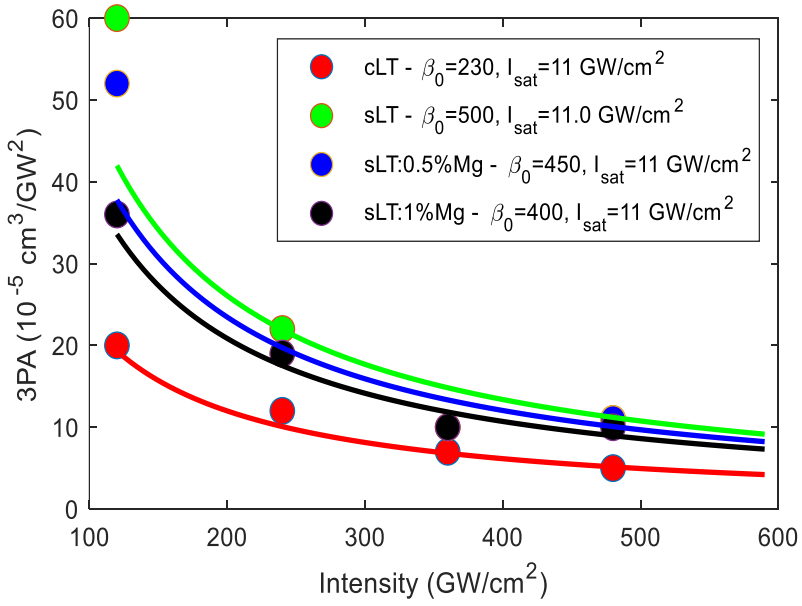

Figure 8-2 Fitting for saturation intensity to the obtained coefficients. I_{sat} in the legend corresponds to the saturation intensity [121].

Table 8-2: Calculated coherence length (l_c) for second harmonic generation (SHG) in both oo-e and ee-e SHG processes in LT crystals. n_o and n_e are the refractive indices for ordinary and extraordinary polarizations, respectively.

Crystal	wavelength (μm)	n_o	n_e	T (K)	Ref	Process	l_c (μm)
sLT	0.8	2.1545	2.1512	293	[114]	oo-e	1.58
	0.4	2.2879	2.2806			ee-e	1.54
sLT:0.5% Mg	0.8	2.1487	2.1464	300	[116]	oo-e	1.60
	0.4	2.2769	2.2734			ee-e	1.57
sLT:1.0% Mg	0.8	2.1545	1.1510	293	[114]	oo-e	1.58
	0.4	2.2828	2.2793	297	[117]	ee-e	1.55
cLT	0.8	2.1538	2.1580			oo-e	1.35
	0.4	2.2879	2.3011			ee-e	1.39

8.3. Comparison

Comparing the three-photon absorption coefficients in LT with LN adds complexity to our understanding. The investigation employed the same method, using the same pump source at 800 nm, and a 40 fs pulse duration. This examination focused on extraordinary polarization, assuming nearly identical intensity levels: LT at I=240 GW/cm² and LN at I=255 GW/cm². Table 8-3 reveals a clear disparity in the absorption coefficients, with LT displaying considerably higher values than LN under the specified conditions. This difference challenges our expectations, given the established scaling law of multiphoton absorption (MPA), which predicts a smaller MPA coefficient for materials with a larger bandgap [118]. Notably, LT with its larger bandgap compared to LN, contradicts this by exhibiting higher three-photon absorption. The nature of this outcome raises questions, and currently, an explanation for this unusual phenomenon remains unclear. Nevertheless, it is important to note that this observation aligns with a known phenomenon in multi-photon (external) photoemission, where emission experiences a substantial increase when the excitation photon energy lies across the boundary of two different orders of multi-photon photoemission [119]. This unexpected behaviour prompts a deeper exploration into the underlying mechanisms governing three-photon absorption in LT and LN. The disparity with the scaling law of MPA and the correlation with multi-photon photoemission boundaries indicate that there may be other factors at play in the interaction of photons with these materials.

Table 8-3. Comparison of the calculated 3PA coefficients of LN and LT for extraordinary polarization at 800 nm wavelength for 255 GW/cm^2 and 240 GW/cm^2 intensity, respectively.

Crystals	$LiNbO_3$						$LiTaO_3$			
	sLN: 4.18% Mg	sLN: 1.50% Mg	sLN: 0.67% Mg	cLN	cLN: 1.0% Mg	cLN: 6.0% Mg	sLT	sLT: 0.5% Mg	sLT: 1.0% Mg	cLT
3PA ($\times 10^{-4}$cm^3/GW^2)	0.36	0.30	0.25	0.33	0.32	0.28	2.2	1.9	1.9	1.2

Chapter Nine: Conclusion

9.1 Conclusion

In conclusion, our study utilized open-aperture Z-scan measurements to investigate three-photon (3PA) and four-photon absorption (4PA) coefficients in lithium niobate and lithium tantalate congruent (cLN, cLT) and stochiometric (sLN, sLT) crystals with different Mg doping concentrations using laser pulses at 800 nm and 1030 nm wavelengths. Notably, we observed distinct variations in 3PA and 4PA coefficients at different Mg doping concentrations with varying intensities. Both cLN and sLN exhibited absorption minima at specific Mg doping concentrations, indicating effective suppression of photo-refraction. This suggests the interplay of second harmonic and defect center-related polarons, providing insights into the underlying mechanisms governing these nonlinear optical phenomena. Additionally, our investigation highlighted differences in nonlinear absorption behavior between 3PA at 800 nm and 4PA at 1030 nm, with the latter showing greater absorption under similar intensity levels. In another aspect of our study, the intensity-dependent 3PA of LT crystals with different compositions and magnesium doping levels at 800 nm pumping wavelength, we found that crystal absorption decreases as intensities increase from 120 GW/cm² to 480 GW/cm². The difference in absorption between differently doped stoichiometric samples is minimal at low pumping intensities, disappearing above 240 GW/cm². Congruent LT demonstrated lower multi-photon absorption, making it more attractive for nonlinear applications such as THz generation. Analyzing 3PA and 4PA coefficients in lithium niobate crystals holds promise for selecting the most suitable crystal type for efficient terahertz (THz) generation and other nonlinear optical processes requiring high pump intensities. However, the comparisons with stoichiometric and congruent LN crystals at the same wavelength and similar pumping intensity revealed that LN is more favorable at 800 nm due to its lower absorption. This study is crucial for identifying optimal nonlinear optical materials for the development of optoelectronics, photonics devices, THz generation, and other nonlinear optical processes.

Chapter Ten: Thesis Statements

10.1Thesis statements

1. Open-aperture Z-scan measurements have been carried out to investigate the possible photon absorption coefficients at 800 nm wavelength, 40 fs pulse duration, and 1 kHz of repetition rate in congruent (cLN, cLT) and stoichiometric (sLN, sLT) lithium niobate and lithium tantalate respectively with different concentrations of Mg doping. The measurements were carried out specifically for extraordinary polarization in lithium niobate crystals, while also accounting for both ordinary and extraordinary polarizations in lithium tantalate crystals. The peak intensity inside the crystals varied between approximately 110 and 550 GW/cm^2. The outcomes reveal that the dominant multi-photon absorption with this pumping wavelength is three-photon absorption (3PA).
2. 3PA coefficients in LN and LT were investigated. The evaluation was carried out by fitting a theoretical curve to the measured points. The 3PA coefficients exhibited distinctive variations at different Mg doping concentrations with different intensities. Both cLN and sLN displayed minima in their absorption coefficients at a specific Mg doping concentration, corresponding to the point at which photo-refraction was effectively suppressed, and have maximum absorption coefficients at about 290 GW/cm^2 for all the investigated LN crystals. For both cLT and sLT crystals, the transmission curves show significantly deeper values for ordinary polarization compared to extraordinary polarization. Consequently, the calculated 3PA coefficients exhibit greater magnitudes under ordinary polarization than under extraordinary polarization, the absorption of LT crystals decreases by increasing intensities from 120 GW/cm^2 to 480 GW/cm^2, and there is only a slight difference in the absorption between the differently doped stoichiometric samples at low pumping intensities which vanishes above 240 GW/cm^2. The congruent LT has lower multi-photon absorption, hence more attractive for nonlinear applications like THz generation.
3. Measurements have been performed to investigate the possible four-photon absorption coefficients in lithium niobate crystals using the open-aperture Z-scan technique. This study employed a femtosecond laser pulse of 190 fs at 1030 nm of central wavelength and 1 kHz of repetition rate. The investigation was carried out on congruent and stoichiometric (cLN, sLN) crystals having different Mg doping

concentrations. Both ordinary and extraordinary polarizations were considered. The crystals were exposed to a pump intensity of 180 GW/cm^2 (considered a practical intensity level) to prioritize the measurement of the absorption coefficients at various polarizations, rather than solely focusing on variations in the coefficient at different intensity levels. The results indicate that the primary multi-photon absorption occurring at this pumping wavelength is not caused by genuine 4PA. Nevertheless, effective 4PA values through the fitting, can be used for designing nonlinear optical applications at the intensities used during measurement.

4. Effective four-photon absorption (4PA) coefficients in LN were investigated at 1030 nm. Both cLN and sLN exhibited minima in their absorption coefficients at specific Mg doping concentrations (sLN: 0.67% Mg and cLN: 6.0% Mg), corresponding to the point where photo-refraction was effectively suppressed. The z-scan curves measured at ordinary polarization indicated significantly larger absorption than those measured for extraordinary polarization. However, the magnesium doping dependence was much stronger than at 800 nm. The 4PA at 1030 nm exhibited greater nonlinear absorption than the 3PA at 800 nm under the same intensity level. This finding indicates the role of the interplay between the second harmonic and defect center-related polarons, shedding light on the underlying mechanisms governing these nonlinear optical phenomena.
5. Comparing the two crystals under similar conditions. Surprisingly, the three-photon absorption (3PA) coefficients were larger for LT than for LN, despite LT having a larger bandgap width than LN. This suggests that LT is not superior to LN in terms of nonlinear optical applications when using 800 nm pumping pulses. This is consistent with the observation that in the case of multi-photon (external) photoemission, emission significantly increases when the excitation photon energy is at the boundary of the two different orders of multi-photon photoemission.

Chapter Eleven: Hungarian summary

11.1 Összefoglaló

11.1.1 Absztrakt

Az elmúlt években figyelemre méltó érdeklődés mutatkozott a többfoton-abszorpciós mechanizmusok iránt. Ez a növekvő érdeklődés annak köszönhető, hogy számos kutatási területen hasznosíthatók, többek között az optikai korlátozásban (optical limiting), adattárolásban és biomedikai kutatásokban. A mai napig az egyik legszélesebb körben kutatott folyamat a kétfoton abszorpció (2PA). Az elmúlt két évtizedben a femtoszekundumos közeli infravörös impulzusok lítium-niobátban (LN, $LiNbO_3$) történő optikai egyenirányítása lett a legelterjedtebb módja a nagyenergiájú terahertzes (THz) impulzusok előállításának a THz-spektrum alacsony (0,1-2 THz) részén. Az LN mellett a lítium-tantalát (LT, $LiTaO_3$), egy másik ferroelektromos kristály ugyanebből a szimmetriaosztályból, szintén érdekes anyag a THz-generálás szempontjából. A közelmúltban jelentős erőfeszítéseket tettek a hagyományos döntött impulzusfrontú pumpálás korlátainak legyőzésére, és részletesebb elméleti modelleket hoztak létre az újonnan javasolt elrendezések teljesítményének összehasonlítására az egyik fő korlátozó tényező a maximálisan használható pumpa intenzitás, amit a pumpa által kiváltott többfotonos abszorpció által okozott szabad töltéshordozók abszorpciója limitál. Ezeknek a korlátoknak a leküzdésére nyitott-apertúrás Z-scan méréseket végeztünk, hogy megvizsgáljuk a háromfotonos (3PA) abszorpciót LN és LT esetében, valamint a négyfotonos abszorpciót (4PA) kongruens (cLN, cLT) és sztöchiometrikus (sLN, sLT) kristályokban 800 nm-es és 1030 nm-es hullámhosszakon, különböző Mg-adalékolásnál. A lézerimpulzus hossza a két hullámhosszon 40 és 190 fs volt, egyaránt figyelembe véve az ordinárius és extraordinárius polarizációt. A kristályokon belüli csúcsintenzitás körülbelül 110 és 555 GW/cm^2 között változott. A 3PA és 4PA együtthatókat egy elméleti modell segítségével értékeltem ki. Az LN kristályok esetében az eredmények azt sugallják, hogy a minimum közel van ahhoz a Mg-szennyezési szinthez, amely megfelel a fotorefrakció elnyomásának küszöbértékének mind a cLN, mind az sLN esetében. Ez az eredmény a kristályhibák hozzájárulásának tulajdonítható a 3PA és 4PA folyamatokban. Továbbá, a 4PA 1030 nm-es hullámhosszon nagyobb nemlineáris abszorpciót mutatott, mint a 3PA 800 nm-es hullámhosszon ugyanazon intenzitási szinten. Ennek a váratlan viselkedésnek lehetséges okait a dolgozatban körüljárom. Az LT kristályok esetében az eredmények

azt mutatják, hogy a domináns többfotonos abszorpció ezen a pumpálási hullámhosszon a háromfotonos abszorpció (3PA), és a 3PA együtthatójának csökkenése mutatható ki a pumpálási intenzitás növekedésével. Meglepő módon nagyobb 3PA együtthatókat mértem LT-nál, mint LN-nál, ellentétben a LT nagyobb tiltottsávjához képest LN-hoz viszonyítva. Összességében ezeknek a kristályoknak a 3PA és 4PA értékeinek összehasonlítása lehetővé teszi a LN és LT kristályok optimális összetételének kiválasztását hatékony THz generáláshoz és más nemlineáris optikai folyamatokhoz, amelyek magas pumpa intenzitást igényelnek.

11.1.2 Tézispontok

1. Nyitott-apertúrás Z-scan méréseket végeztem annak érdekében, hogy megvizsgáljam a lehetséges fotonabszorpciós együtthatókat 800 nm hullámhosszon, 40 fs-os impulzushosszon és 1 kHz ismétlési frekvenciával kongruens (cLN, cLT) és a sztoichiometrikus (sLN, sLT) lítium niobátban és lítium tantalátban különböző Mg-adalékolással. A méréseket kifejezetten az extraordinárius polarizációra vonatkozóan végeztem el a lítium niobát kristályok esetében, miközben mind az ordinárius, mind az extraordinárius polarizációkat figyelembe vettem a lítium tantalát kristályok esetében. A kristályokon belüli csúcsintenzitás körülbelül 110 és 550 GW/cm2 között változott. Az eredmények azt mutatják, hogy a domináns többfotonos abszorpció ezen a pumpálási hullámhosszon a háromfotonos abszorpció (3PA).
2. Meghatároztam LN és LT háromfotonos abszorpciós együtthatóit (3PA). Az értékelés egy elméleti görbe illesztésével történt a mért pontokhoz. A 3PA együtthatók jellegzetes változásokat mutattak különböző Mg-adalékolásnál és különböző intenzitásoknál. Mind a cLN, mind az sLN kristályok olyan Mg-adalékolásnál mutattak minimumot az abszorpciós együtthatókban, ami megfelel a fotorefrakciós hatás kiküszöbölésének. Mindkét összetételű LN kristálynál 290 GW/cm2 intenzitásnál mértem maximum abszorpciós együtthatót. Mind a cLT, mind az sLT kristályok esetében a transzmissziós görbék lényegesen mélyebb értékeket mutatnak az ordinárius polarizációhoz képest az extraordinárius polarizációhoz viszonyítva. Ennek megfelelően a számított 3PA együtthatók nagyobb nagyságrendeket mutatnak az ordinárius polarizáció alatt, mint az extraordinárius polarizáció alatt. Az LT kristályok abszorpciója csökken az intenzitás növekedésével 120 GW/cm2-től 480 GW/cm2-ig, és csak csekély

különbség van az abszorpcióban a különböző módon adalékolt sztöchiometrikus minták között alacsony pumpálási intenzitásoknál, ami eltűnik 240 GW/cm2 felett. A kongruens LT alacsonyabb többfotonos abszorpcióval rendelkezik, ezért vonzóbb a nemlineáris alkalmazások számára, például a THz-keltés szempontjából.

3. 1030 nm pumpáló hullámhosszon vizsgáltam különböző adalékolású és összetételű LN kristályok többfotonos abszorpciós együtthatóit nyitott-apertúrás Z-scan mérésekkel, 190 fs-os impulzusok felhasználásával 1 kHz ismétlési frekvencián. A vizsgálatot kongruens és sztoichiometrikus (cLN, sLN) kristályokon végeztem, amelyek különböző Mg-adalékolással rendelkeztek. Mind az ordinárius, mind az extraordinárius polarizációkat figyelembe vettem. A kristályokat 180 GW/cm2-es intenzitással pumpáltam (ami gyakorlatias intenzitási szintnek tekinthető), hogy elsődlegesen különböző polarizációkkal mérjek abszorpciós együtthatókat, ahelyett, hogy kizárólag a különböző intenzitási szintekben lévő együtthatók változására összpontosítanék. Az eredmények azt mutatják, hogy a fő többfotonos abszorpció ezen a pumpálási hullámhosszon nem tisztán négyfotonos természetű. Mindazonáltal effektív négyfotonos abszorpciós értékeket határoztam meg illesztések révén, amelyek felhasználhatók nemlineáris optikai alkalmazások tervezésére a mérések során használt intenzitásoknál.
4. Megmutattam, hogy az effektív négyfotonos abszorpciós (4PA) együtthatóknak minimuma van azon Mg-adalékolásoknál (sLN: 0,67% Mg és cLN: 6,0% Mg), amelyeknél a legkisebb a fotorefrakció. Az ordinárius polarizációnál mért Z-scan görbék lényegesen nagyobb abszorpciót mutattak, mint az extraordinárius polarizáción mért görbék, azonban a magnézium adalékolástól való függés sokkal erősebb volt, mint 800 nm-nél. A 4PA 1030 nm-en nagyobb nemlineáris abszorpciót mutatott, mint a 3PA 800 nm-en ugyanazon intenzitási szinten. Ez az eredmény azt jelzi, hogy a másodharmonikus és a hibahelyekhez kapcsolódó polaronok közötti kölcsönhatásoknak szerepe van ezekben a folyamatokban.
5. Összehasonlítottam a két kristályt hasonló körülmények között. Meglepő módon a háromfotonos abszorpciós (3PA) együtthatók nagyobbak voltak LT esetében, mint LN esetében, annak ellenére, hogy LT nagyobb tiltott sávszélességgel rendelkezik, mint LN. Ez arra utal, hogy LT nem jobb LN-hoz képest nemlineáris optikai alkalmazásokat tekintve, ha 800 nm-es pumpáló impulzusokat használnak. Ez összhangban van azzal a megfigyeléssel, miszerint a többfotonos (külső)

fotoemisszió esetén a kibocsátás jelentősen megnő, amikor a gerjesztési fotonenergia a többfotonos fotoemisszió két különböző rendjének határán van.

Chapter Twelve: English summary

12.1 Summary

12.1.1 Introduction

In the past two decades optical rectification of femtosecond near-infrared pulses in lithium niobate (LN or $LiNbO_3$) has become the most widespread way to generate high energy terahertz (THz) pulses in the low part of the THz spectrum (0.1 – 2 THz) leading to the generation of both high-energy broadband THz pulses [5-7] and narrowband radiation [8-10]. The success of OR can be attributed to several critical factors. One key element is the substantial difference in the indices of refraction between the near-infrared laser light used for pumping and the THz waves. This difference enables the efficient conversion of the pumped energy into THz radiation. The process of quasi-phase matching, achieved through periodic poling of the crystalline material [12], as well as velocity matching through tilted-pulse-front pumping [13] plays an important role in enhancing the conversion efficiency for both narrowband and broadband pulse generation. However, a crucial challenge associated with OR and similar frequency conversion processes is particularly related to the nonlinear absorption phenomenon. This phenomenon has been observed in various materials [120], with a specific focus on multi-photon absorption (MPA) [16,17] and free-carrier absorption (FCA) [17]. LN possesses a relatively large bandgap of around 3.8 eV [34,35]. These properties are crucial in making LN suitable for nonlinear optical applications. In terms of its nonlinear optical properties, LN exhibits an exceptionally high damage threshold of 204 GW/cm^2 for short 1 ps pulses with a repetition rate of 10 kHz [46]. Similar to LN crystal, lithium tantalate, (LT or $LiTaO_3$), is an isomorph of LN where the Ta^{5+} ion replaces the Nb^{5+} ion [56] with a relatively large band gap of 4.9 eV [57]. It is a material of interest and promising in terms of THz generation through nonlinear optical processes also due to its excellent optical and electronic properties [66], large nonlinear coefficients, and high damage thresholds. Several studies have been conducted on the determination of MPA coefficients in LN and LT crystals using different techniques. However, the Z-scan setup originally introduced by Sheik-Bahae et al [19] is a reliable and accurate method for measuring MPA coefficients in these materials. This technique involves measuring the transmission of a material as a function of the sample's position along the optical axis. A simple transmission measurement was used to determine the 2PA [20] in LN. However, 2PA coefficients and third-order nonlinear refractive index

of LT were determined using the Z-scan setup [25], also another study investigated 2PA in undoped sLT crystals [26] and congruent crystals [27]. The Z-scan technique was applied to evaluate the 3PA in LN [21] and used to investigate the scanning nonlinear absorption in LN over the time regime of small polaron formation [22]. However, 3PA coefficients have not been determined yet in LT. In a previous study, 4PA in LN was estimated based on the saturation of THz pulse generation efficiency with increasing pump intensity [23]. Recently, a simple transmission measurement was used to determine the 4PA coefficient of stoichiometric LN [24]. Notably, 4PA of LN has not yet been measured using the Z-scan technique. These investigations into the nonlinear optical properties of LN and LT are crucial for understanding and optimizing its performance in a range of applications.

12.1.2 Objectives and methods

LN crystals have large effective nonlinear coefficients which are advantageous for the generation of THz pulses by optical rectification. LT, which belongs to the same symmetry class as ferroelectric crystals, is also a noteworthy material for generating THz radiation. However, there exist difficulties in increasing the scale of THz pulse energies and field strengths, such as the free-carrier absorption in the THz range induced by the multiphoton absorption of the pump. The experimental work carried out during this thesis was based on the research lines being conducted at two laboratories: the High-Field Terahertz (THz) Laboratory at the Institute of Physics, Szentágothai Research Centre, and at the Ultrafast High-Intensity Light-Matter Interactions Laboratory at the Institute for Solid State Physics and Optics, Wigner Research Centre. In accordance with them, the general objective consisting of proposing and implementing feasible solutions to the challenges involved in the precise processing of materials with two different laser sources was set out.

More specifically, the following main objectives were proposed: The main aim of this work was to determine multiphoton absorption coefficients in lithium niobate and lithium tantalate crystals by the Z-scan technique consisting of two different femtosecond laser sources. My first goal was to investigate 3PA coefficients in LN crystals. I planned to use the open aperture Z-scan technique which consisted of a Ti:shappire laser (Newport-Spectra Physics) producing 40 fs long pulses at 800 nm and 1 kHz of repetition rate in LN congruent (cLN) and stoichiometric (sLN) crystals at different Mg-doping concentrations for extraordinary polarization. The peak intensity

inside the crystals varied between approximately 110 and 550 GW/cm^2. The second objective of the study was the determination of 3PA coefficients in LT crystals. by using the same laser parameters with a similar process in undoped congruent, undoped, and Mg-doped stoichiometric LT crystals (cLT, sLT) for both ordinary and extraordinary polarized light. The peak intensity inside the crystals varied between approximately 120 and 480 GW/cm^2. The third objective was to measure the 4PA coefficients in LN crystals. I planned to use the open aperture Z-scan technique which consisted of an Yb laser (Pharos, Light Conversion) producing 190 fs long pulses at 1030 nm at 1 kHz repetitions rate in LN congruent (cLN) and stoichiometric (sLN) crystals at different Mg-doping concentrations for both ordinary and extraordinary polarization. The peak intensity inside the crystals was 180 GW/cm^2. The fourth objective was to identify the optimum crystal composition for efficient THz generation and other nonlinear optical processes requiring high pump intensities, I made a comparison between the 3PA coefficients in LN and LT crystals, using the same pump source at 800 nm, and a 40 fs pulse duration. This examination focused on extraordinary polarization, assuming nearly identical intensity levels: LT at I=240 GW/cm² and LN at I=255 GW/cm².

12.1.3 New scientific results

I. I performed open-aperture Z-scan measurements at 800 nm wavelength, 40 fs pulse duration, and 1 kHz of repetition rate in congruent (cLN, cLT) and stoichiometric (sLN, sLT) lithium niobate and lithium tantalate with different concentrations of Mg doping. I carried out the measurements specifically for extraordinary polarization in LN, while also accounting for both ordinary and extraordinary polarizations in LT crystals. The peak intensity inside the crystals varied between approximately 110 and 550 GW/cm^2. I have demonstrated the possible photon absorption coefficients, since LN has a band-gap of about 3.8 eV, the maximum wavelength where 3PA is possible is about $\lambda_{3PA} = 3hc/E_g = 980\,nm$. Beyond that I considered the E_g = 4.9 eV optical band gap of LT as mentioned earlier, I expected border wavelength between 3PA and 4PA ranges at $\lambda_P = 3hc/E_g = 761\,nm$. I have concluded that the dominant multi-photon absorption with this pumping wavelength is three-photon absorption (3PA) [S1, S2].

II. Using the pulse propagation model by fitting a theoretical curve to the measured points I have investigated 3PA coefficients in LN and LT. I have shown that the 3PA coefficients exhibited distinctive variations at different Mg doping concentrations with different intensities. For all the investigated LN crystals composition I have shown that both cLN and sLN displayed minima in their absorption coefficients at a specific Mg doping concentration, corresponding to the point at which photo-refraction was effectively suppressed, and have maximum absorption coefficients at about 290 GW/cm^2. In the case of LT for both cLT and sLT crystals, the transmission curves show significantly deeper values for ordinary polarization compared to extraordinary polarization. Consequently, I have shown that the calculated 3PA coefficients exhibit greater magnitudes under ordinary polarization than under extraordinary polarization, the absorption of LT crystals decreases by increasing intensities from 120 GW/cm^2 to 480 GW/cm^2. I have shown that there is only a slight difference in the absorption between the differently doped stoichiometric samples at low pumping intensities which vanishes above 240 GW/cm^2. Furthermore, the congruent LT has lower multi-photon absorption, hence more attractive for nonlinear applications like THz generation [S1, S2].

III. To investigate the possible photon absorption coefficients in lithium niobate crystals I carried out the open-aperture Z-scan technique at 1030 nm of central wavelength, femtosecond laser pulse of 190 fs, and 1 kHz of repetition rate on congruent and stoichiometric (cLN, sLN) crystals having different Mg doping concentrations. Both ordinary and extraordinary polarizations were considered. I considered a practical pump intensity level of 180 GW/cm^2 to prioritize the measurement of the absorption coefficients at various polarizations, rather than solely focusing on variations in the coefficient at different intensity levels. I examined the pulse propagation model by fitting a theoretical curve to the measured points. I pointed out that the primary multi-photon absorption occurring at this pumping wavelength is not caused by genuine 4PA. Nevertheless, effective 4PA values through the fitting, can be used for designing nonlinear optical applications at the intensities used during measurement [S1].

IV. I determined the effective four-photon absorption (4PA) coefficients in LN investigated at 1030 nm. I found that both cLN and sLN exhibited minima in their absorption coefficients at specific Mg doping concentrations (sLN: 0.67% Mg and

cLN: 6.0% Mg), corresponding to the point where photo-refraction was effectively suppressed. I have shown that the z-scan curves measured at ordinary polarization indicated significantly larger absorption than those measured for extraordinary polarization. However, the magnesium doping dependence was much stronger than at 800 nm. I also verified the 4PA at 1030 nm exhibited greater nonlinear absorption than the 3PA at 800 nm under the same intensity level. I concluded this finding with the role of the interplay between the second harmonic and defect center-related polarons, shedding light on the underlying mechanisms governing these nonlinear optical phenomena [S1, S2].

V. I compared the 3PA for both LN and LT at 800 nm by supposing identical pump intensity. I have shown that larger 3PA coefficients were measured for LT than for LN, contrary to the larger bandgap of LT in comparison to LN. I concluded that LT has no advantage in comparison to LN in nonlinear optical applications if 800 nm pump pulses are used. As the explanation for this unusual phenomenon, I noted that it is consistent with the observation that in multi-photon (external) photoemission, the emission significantly increases when the excitation photon energy is at the boundary of two different orders of multi-photon photoemission [S1, S2].

List of Publications

Publications related to the dissertation

[S1] **I. Benabdelghani**, G.Tóth, G. Krizsán, G. Bazsó, Z. Szaller, N. Mbithi, P. Rácz, P. Dombi, G. Polónyi, and János Hebling, “Three-photon and four-photon absorption in lithium niobate measured by the Z-scan technique”, Optics Express. 32(5), 7030-7043 (2024).

[S2] I. Benabdelghani, G. Bazsó, G.Tóth, P. Rácz, P. Dombi, János Hebling, and G. Polónyi, “Three-photon absorption in lithium tantalate measured by the Z-scan technique”, Optical materials. Submitted, (2024).

Presentations

[E1] **I. Benabdelghani**, V. Gupta, A. Sharma, A. Gupta, G. Á. Polónyi, J. Hebling, J. A. Fülöp, "Terahertz pump transmission measurements in lithium niobate", 10th Jubilee Interdisciplinary Doctoral Conference, 347 297 (2021).

[E2] **I. Benabdelghani**, G. Krizsán, L. Nasi, N. M. Mbithi, J. A. Fülöp, "Measurements of four-photon absorption in lithium niobate", 1st International Conference on Sustainable Energy and Advanced Materials, (2021).

[E3] **I. Benabdelghani**, L. Nasi, G. Tóth, L. Pálfalvi, J. Hebling, G. Krizsán, "Measurement of Four Photon Absorption Coefficient in Lithium Niobate by Z-scan Technique", 9th International Conference on Applications of Femtosecond Lasers in Materials Science, (2022).

[E4] **I. Benabdelghani**, G.Tóth, G. Krizsán, N. Mbithi, G. Bazsó, P. Rácz, P. Dombi, J. Hebling, G. Polónyi, "Three-photon and Four-photon Absorption in Lithium Niobate and Lithium Tantalate by Z-scan Technique", Lasers and Electro-Optics Europe & European Quantum Electronics Conference (CLEO/Europe-EQEC), (2023).

[E5] G. Polónyi, G. Tóth, N. Mbithi, Z. Tibai, **I. Benabdelghani**, L. Nasi, G. Krizsán, G. Illés, J. Hebling, "Investigation of Terahertz Pulse Generation in Semiconductors Pumped at Long Infrared Wavelengths", Lasers and Electro-Optics Europe & European Quantum Electronics Conference (CLEO/Europe-EQEC), (2023).

Other publications

[S3] N. M. Mbithi, G. Tóth, Z. Tibai, **I. Benabdelghani**, L. Nasi, G. Krizsán, J. Hebling, and G. Polonyi, "Investigation of terahertz pulse generation in semiconductors pumped at long infrared wavelengths," J. Opt. Soc. Am. B, 39(10), 2684-2691 (2022).

References

1. J. F. Federici, B. Schulkin, F. Huang, D. Gary, R. Barat, F. Oliveira, D. Zimdars, “THz imaging and sensing for security applications-explosives, weapons and drugs,” Semicond. Sci. Technol. 20(7), S266–S280 (2005).
2. M. C. Kemp, P. F. Taday, B. E. Cole, J. A. Cluff, A. J. Fitzgerald and W. R . Tribe “Security applications of terahertz technology,” Proc. SPIE. 5070, 44–52 (2003).
3. A. Boes, L. Chang, C. Langrock, M. Yu, M. Zhang, Q. Lin, M. Lončar, M. Fejer, J. Bowers, A. Mitchell, “Lithium niobate photonics: Unlocking the electromagnetic spectrum,” Science 379(6627), 4396 (2023).
4. Z. Ma, P. Li, S. Chen, X. Wu, “Optical generation of strong-field terahertz radiation and its application in nonlinear terahertz metasurfaces,” Nanophotonics. 11(9), 1847–1862 (2022).
5. M. Nagai, M. Jewariya, Y. Ichikawa, H. Ohtake, T. Sugiura, Y. Uehara, and K. Tanaka, “Broadband and high power terahertz pulse generation beyond excitation bandwidth limitation via χ(2) cascaded processes in LiNbO3,” Opt. Express. 17(14), 11543–11549 (2009).
6. B. Zhang, Z. Ma, J.-L. Ma, X.-J. Wu, C. Ouyang, D. Kong, T. Hong, X. Wang, P. Yang, L. Chen, Y. Li, J. Zhang, “1.4 mJ high energy terahertz radiation from lithium niobates,” Las. & Phot. Rev. 15(3), 1–11 (2021).
7. L. Carletti, C. McDonnell, U. A. Leon, D. Rocco, M. Finazzi, A. Toma, T. Ellenbogen, G. D. Valle, M. Celebrano, and C. D. Angelis, “Nonlinear THz Generation through Optical Rectification Enhanced by Phonon–Polaritons in Lithium Niobate Thin Films,” ACS Photonics. 10(9), 3419–3425 (2023).
8. S. Carbajo, J. Schulte, X. Wu, K. Ravi, D. N. Schimpf, and F. X. Kärtner, “Efficient narrowband terahertz generation in cryogenically cooled periodically poled lithium niobate,” Opt. Lett. 40(24), 5762–5765 (2015).
9. F. Ahr, S. W. Jolly, N. H. Matlis, S. Carbajo, T. Kroh, K. Ravi, D. N. Schimpf, J. Schulte, H. Ishizuki, T. Taira, A. R. Maier, and F. X. Kärtner, “Narrowband terahertz generation with chirped-and-delayed laser pulses in periodically poled lithium niobate,” Opt. Lett. 42(11), 2118–2121 (2017).
10. F. Lemery, T. Vinatier, F. Mayet, R. Assmann, E. Baynard, J. Demailly, U. Dorda, B. Lucas, A.-K. Pandey, M. Pittmann, “Highly scalable multicycle terahertz production with a homemade periodically poled macrocrystal,” Commun. Phys. 3(1), 150 (2020).
11. S. W. Huang, E. Granados, W. R. Huang, K. H. Hong, L. E. Zapata, and F. X. Kärtner, “High conversion efficiency, high energy terahertz pulses by optical rectification in cryogenically cooled lithium niobate,” Optics Lett. 38(5), 796–798 (2013).
12. Y.-S. Lee, T. Meade, V. Perlin, H. Winful, T. B. Norris, and A. Galvanauskas, “Generation of narrow-band terahertz radiation via optical rectification of femtosecond pulses in periodically poled lithium niobate,” Appl. Phys. Lett 76(18), 2505–2507 (2000).
13. J. Hebling, G. Almási, I. Z. Kozma, and J. Kuhl, “Velocity matching by pulse front tilting for large area THz-pulse generation,” Opt. Express. 10(21), 1161–1166 (2002).
14. G. Tóth, G. Polónyi, and J. Hebling, “Tilted pulse front pumping techniques for efficient terahertz pulse generation,” Light Sci Appl. 12(1), 256 (2023).
15. G. Krizsán, Z. Tibai, J. Hebling, L. Pálfalvi, G. Almási, and G. Tóth, “Lithium niobate and lithium tantalate-based scalable terahertz pulse sources in reflection geometry,” Opt. Express. 28(23), 34320–34327 (2020).
16. V. Nathan, A. H. Guenther, and S. S. Mitra, “Review of multiphoton absorption in crystalline solids,” JOSA B. 2(2), 294–316 (1985).
17. T. Kawamori, P. G. Schunemann, V. Gruzdev, and K. L. Vodopyanov, “High-order (N = 4 - 6) multiphoton absorption and mid-infrared Kerr nonlinearity in GaP, ZnSe, GaSe, and ZGP crystals,” APL Photon 7(8), 086101 (2022).

18. A. Srinivasa Rao, “Saturation effects in nonlinear absorption, refraction, and frequency conversion: a review,” Optik Volume. 267, 169638 (2022).
19. M. Sheik-Bahae, A. A. Said, T. Wei, D. J. Hagan, and E. W. Van Stryland, “Sensitive measurement of optical nonlinearities using a single beam,” IEEE J. Quantum Electron. 26(4), 760–769 (1990).
20. O. Beyer, D. Maxein, K. Buse, B. Sturman, H. T. Hsieh, and D. Psaltis, “Femtosecond time-resolved absorption processes in lithium niobate crystals,” Optics Lett. 30(11), 1366–1368 (2005).
21. H. P. Li, J. K. Liao, X. G. Tang, W. Ji, “Three-photon absorption in MgO-doped LiNbO3 crystal,” in CLEO/QELS 2008 JWA35 (2008).
22. H. Badorreck, S. Nolte, F. Freytag, P. Bäune, V. Dieckmann, and M. Imlau, “Scanning nonlinear absorption in lithium niobate over the time regime of small polaron formation,” Opt. Materials Express. 5(12) 2729–2741 (2015).
23. M. C. Hoffmann, K.-L. Yeh, J. Hebling, and K. A. Nelson, “Efficient terahertz generation by optical rectification at 1035 nm,” Opt. Express. 15(18), 11706–11713 (2007).
24. M. V. Tsarev, D. Ehberger, and P. Baum, “High-average-power, intense THz pulses from a LiNbO3 slab with silicon output coupler,” Appl. Phys. B. 122(2), 30 (2016).
25. D. Guichaoua, I. Syvorotka, I. Solskii, N. Syvorotka, K. Waszkowska, A. Andrushchak, B. Sahraoui, “Specific complex-oxide crystals with strong nonlinear absorption and nonlinear refraction as promising optical materials,” Opt. Materials. 121, 111493 (2021).
26. I. S. Steinberg, A. V. Kirpichnikov, and V. V. Atuchin, “Two-photon absorption in undoped LiTaO3 crystals,” Opt. Mater. 78, 253–258 (2018).
27. I.S. Steinberg, V.V. Atuchin, “Two-photon holographic recording in LiTaO3:Fe crystals with high-intensity nanosecond pulses at 532 nm,” Materials. Chem. Phys. 253(23), 122956 (2020).
28. A. Rauber, “Current Topics in Material Sciences,” North-Holland. Amsterdam. 1, 481–600 (1978).
29. G. Stone, B. Knorr, V. Gopalan, and V. Dierolf, “Frequency shift of Raman modes due to an applied electric field and domain inversion in LiNbO3,” Phys. Rev. B. 84,134303 (2011).
30. M. D. Fontana, and P. Bourson, “Microstructure and defects probed by Raman spectroscopy in lithium niobate crystals and devices,” Appl.Phys.Rev. 2(4), 040602 (2015).
31. P. S. Zelenovskiy, V. Y. Shur, P. Bourson, M. D. Fontana, D. K. Kuznetsov, and E. A. Mingaliev, “Raman study of neutral and charged domain walls in lithium niobate,” Ferroelectrics 398(1), 34–41 (2010).
32. R. M. Araujo, ME. G. Valerio, and R. A. Jackson, “Computer simulation of metal co-doping in lithium niobate,” Proc. R. Soc. A. 470, 20140406 (2014).
33. R. S. Weis and T. K. Gaylord, “Lithium niobate: Summary of physical properties and crystal structure,” Appl Phys A. 37(4), 191–203 (1985).
34. A. R. Zanatta, “The optical bandgap of lithium niobate (LiNbO3) and its dependence with temperature,” Results. Phys. 39, 105736 (2022).
35. K. Lengyel, Á Péter, L. Kovács, G. Corradi, L. Pálfalvi, J. Hebling, M. Unferdorben, G. Dravecz, I. Hajdara, Z. Szaller, and K. Polgár, “Growth, defect structure, and THz application of stoichiometric lithium niobate,” Appl. Phys. Rev. 2(4), 040601 (2015).
36. O. Sánchez-Dena, C. D. Fierro-Ruiz, S. D. Villalobos-Mendoza, D. M. Carrillo Flores, J. T. Elizalde-Galindo, and R. Farías, “Lithium Niobate Single Crystals and Powders Reviewed—Part I,” Crystals. 10(11), 973 (2020).
37. K. K. Wong, “Properties of Lithium Niobate,” EMIS Data Reviews Series, INSPEC, Exeter (2002).
38. B. Riscob, I. Bhaumik, S. Ganesamoorthy, R. Bhatt, N. Vijayan, K. Zimik, A. K. Karnal, G. Bhagavannarayana and P. K. Gupta, “Crystal growth of Ru-doped

congruent LiNbO3 and investigation of crystalline perfection and optical properties," J. Appl. Cryst. 48, 1753-1760 (2015).
39. H. M. O'Bryan, P. K. Gallagher, and C. D. Brandle, "Congruent Composition and Li-Rich Phase Boundary of LiNbO3," J. Am. Ceram. Soc. 68(9), 493–496 (1985).
40. S. Uda, C. Koyama, "The population and activity of oxygen in the diffusion boundary layer within a congruent LiNbO3 melt," J. Crys. Growth. 548, 125837 (2020).
41. Y. Li, W.G. Schmidt, S. Sanna, "Intrinsic LiNbO3 point defects from hybrid density functional calculations," Phys. Rev. B. 89(9), 094111 (2014).
42. K. Niwa, Y. Furukawa, S.Takekawa, K. Kitamura, "Growth and characterization of MgO doped near stoichiometric LiNbO3 crystals as a new nonlinear optical material," Journal of Crystal Growth. 20(4), 493–500, (2000).
43. D. A. Bryan, R. Gerson, and H. E. Tomaschke, "Increased optical damage resistance in lithium niobate," Appl. Phys. Lett. 44(9), 847–849 (1984).
44. M. Nakamura, S. Higuchi, S. Takekawa, K.Terabe, Y. Furukawa, and K. Kitamura, "Optical Damage Resistance and Refractive Indices in Near-Stoichiometric MgO-Doped LiNbO3," Jpn. J. Appl. Phys. 41(1), 49–51 (2002).
45. Y. Furukawa, K. Kitamura, S. Takekawa, K. Niwa, and H. Hatano, "Stoichiometric Mg:LiNbO3 as an effective material for nonlinear optics," Opt. Lett. 23(4), 1892–1894 (1998).
46. F. Bach, M. Mero, M.-H. Chou, and V. Petrov, "Laser induced damage studies of LiNbO3 using 1030-nm, ultrashort pulses at 10-1000 kHz," Opt. Mater. Express. 7(1), 240–252 (2017).
47. A. Fedotova, L. Carletti, A. Zilli, F. Setzpfandt, I. Staude, A. Toma, M. Finazzi, C. De Angelis, T. Pertsch, D. N. Neshev, and M. Celebrano, "Lithium Niobate Meta-Optics," ACS Photonics. 9(12), 3745–3763 (2022).
48. J. Hebling, A. G. Stepanov, G. Almási, B. Bartal, and J. Kuhl, "Tunable THz pulse generation by optical rectification of ultrashort laser pulses with tilted pulse front," Appl. Phys. B. 78(5), 593–599 (2004).
49. A. Hellwig, "Nonlinear Optical and Photorefractive Properties of Periodically Poled Channel Waveguides in Lithium," Dissertation, Department Physik der Universität Paderborn zur (2011).
50. E. Hüger, L. Riedel, J. Zhu, J. Stahn, P. Heitjans, and H. Schmidt, "Lithium Niobate for Fast Cycling in Li-ion Batteries: Review and New Experimental Results," Batteries. 9(5), 244 (2023).
51. D. A. Kleinman, "Nonlinear dielectric polarization in optical media," Phys. Rev. 126(6), 1977–1979 (1962).
52. I. Shoji, T. Kondo, A. Kitamoto, M. Shirane, and R. Ito, "Absolute scale of second-order nonlinear-optical coefficients," Opt. Soc. Am. B. 14(9), 2268–2294 (1997).
53. A. Yariv, "Quantum Electronics," John Wiley, 3rd edition (1989).
54. R.W. Boyd, "Nonlinear Optics," Academic Press, 2nd edition (2003).
55. V. Y. Shur, "Lithium niobate and lithium tantalate-based piezoelectric materials," Advanced Piezoelectric Materials Science and Technology. 204–38 (2010).
56. L. Brehmer, Y. Kaminorz, R. Dietel, G. Grasnick and G. Herkner, "Frontiers in Biosensorics I: Fundamental Aspects," ed F. W. Scheller, F. Schubert and J. Fedrowitz (Basel: Birkhäuser Verlag) 155–166 (1997).
57. S. Kase, K. Ohi, "Optical absorption and interband Faraday rotation in LiTaO3 and LiNbO3," Ferroelectrics. 8(1), 419–420 (1974).
58. G. G. Bentini, M. Bianconi, A. Cerutti, M. Chiarini, G. Pennestrì, C. Sada, N. Argiolas, M. Bazzan, P. Mazzoldi, and R. Guzzi, "Structural and compositional characterization of X-cut LiNbO3 crystals implanted with high energy oxygen and carbon ions," Nucl. Instrum. Methods Phys. Res. 240(2), 174–177 (2005).
59. S. Sanna, and W. G. Schmidt, "Lithium niobate X-cut, Y-cut, and Z-cut surfaces from ab initio theory," Phys. Rev. B. 81(2), 214116 (2010).
60. S. Rode, R. Hölscher, S. Sanna, S. Klassen, K. Kobayashi, H. Yamada, W. G. Schmidt, and A. Kühnle, "Atomic-resolution imaging of the polar (0001¯) surface of LiNbO3 in

aqueous solution by frequency modulation atomic force microscopy," Phys. Rev. B. 86(7), 075468 (2012).
61. A. Krampf, M. Imlau, Y. Suhak, H. Fritze, and S. Sanna, "Evaluation of similarities and differences of LiTaO3 and LiNbO3 based on high-T conductivity, nonlinear optical fs-spectroscopy and ab initio modeling of polaronic structures," New J. Phys. 23 033016 (2021).
62. T. Volk, and M. Wöhlecke, "Lithium Niobate: Defects, Photorefraction, and Ferroelectric Switching," Materials Science. 115, (2009).
63. X. Xiao, S. Liang, J. Si, Q. Xu, H. Zhang, L. Ma, C. Yang, and X. Zhang, "Performance of LiTaO3 Crystals and Thin Films and Their Application," Crystals. 13(8), 1233 (2023).
64. S. N. Zhu, Y. Y. Zhu, H. F. Wang, Z. Y. Zhang, N. B. Ming, W. Z.Shen, Y. Chang, X. C. Shen, "Second-order quasi-phase-matched blue light generation in a bulk periodically poled LiTaO3," J. Phys. D Appl. Phys. 28, 2389–2391(1995).
65. G. L. Tangonan, M. K. Barnoski, J. F. Lotspeich, A. Lee, "High optical power capabilities of Ti-diffused LiTaO3 waveguide modulator structures," Appl. Phys. Lett. 30, 238–239 (1977).
66. A. Buzády, M. Unferdorben, G. Tóth, J. Hebling, I. Hajdara, L. Kovács, L. Pálfalvi, "Refractive Index and Absorption Coefficient of Undoped and Mg-Doped Lithium Tantalate in the Terahertz Range," J. Infrared Millim. Terahertz Waves. 38, 963–971 (2017).
67. R. Hsu, E.N. Maslen, D. du Boulay, N. Ishizawa, "Synchrotron X-ray studies of LiNbO3 and LiTaO3,", Acta Cryst. B. 53, 420–428 (1997).
68. V.V. Atuchin, B.I. Kidyarov, N.V. Pervukhina, "Phenomenological modeling and design of new acentric crystals for optoelectronics," Comput. Mater. Sci. 30(4), 411–418 (2004).
69. B. I. Kidyarov, V. V. Atuchin, "Universal Crystal Classification System: Point Symmetry–Physical Property," Ferroelectrics. 360(1), 96–99 (2007).
70. A. A. Blistanov, V. S. Bondarenko, N. V. Perelomova, F. N. Strizhevskaia, V. V. Chkalova, M. P. Shaskolskaia, "Acoustic Crystals," Moscow. Izdatel'stvo Nauka, 632 (1982).
71. M. J. Weber, "Handbook of Optical Crystals: Laser, Optical Science, Technology," CRC Press. 1st edition, (2003).
72. T. C. Ozawa, S. J. Kang, "Balls&Sticks: easy-to-use structure visualization and animation program," J. Appl. Cryst. 37 679 (2004).
73. B. I. Sturman and V. M. Fridkin, "The Photovoltaic and Photorefractive Effects in Noncentrosymmetric Materials," Ferroelectricity and Related Phenomena. 8, (1992).
74. F. Holtmann, J. Imbrock, C. Baumer, H. Hesse, E. Kratzig, and D. Kip, "Photorefractive properties of undoped lithium tantalate crystals for various composition," J. Appl. Phys., 96(12), 7455–7459 (2004).
75. S. Kurimura, S. V. Tovstonog, R. Watanabe, and K. Kitamura, "Periodically poled stoichiometric lithium tantalate for pure blue light generation," In Conference on Lasers and Electro-Optics, CML3, OSA, Long Beach, USA (2006).
76. A. F. Penna, A. Chaves, P. da R. Andrade, and S. P. S. Porto, "Light scattering by lithium tantalate at room temperature," Phys. Rev. B. 13(11), 4907 (1976).
77. P. A. Franken, A. E. Hill, C. Peters, and G. Weinreich, "Generation of optical harmonics," Physical review letters. 7(4), 118–119 (1961).
78. J. Hecht, "A short history of laser development," Applied optics. 49(25), 99–122. (2010).
79. R. W. Boyd, "Nonlinear Optics," 3rd edition. 2–4 (2008).
80. J. A. Fülöp, L. Pálfalvi, S. Klingebiel, G. Almási, F. Krausz, S. Karsch, and J. Hebling, "Generation of sub-mJ terahertz pulses by optical rectification," Opt. Lett. 37(4), 557–559 (2012).
81. J. Fülöp, L. Pálfalvi, G. Almási, and J. Hebling, "Design of high-energy terahertz sources based on optical rectification," Opt. express 18, 12311-12327 (2010).

82. W. T. Hill, and C. H. Lee, “Light-Matter Interaction: Atoms and Molecules in External Fields and Nonlinear Optics,” (2003).
83. R. Boyd, Nonlinear Optics. 4th Edition, Elsevier (2019).
84. Z. H. Amber, B. Kirbus, L. M. Eng, M. Rüsing, “Quantifying the coherent interaction length of second-harmonic microscopy in lithium niobate-confined nanostructures,” J. Appl. Phys. 130 (13), 133102 (2021).
85. A. Tehranchi, “Broadband quasi-phase-matched wavelength converters,” école polytechnique de montréal. Université de montréal. (2010).
86. P. F. Goldsmith, “Quasioptical Systems: Gaussian Beam Quasioptical Propagation and Applications,” Wiley-IEEE Press. (1998).
87. A. E. Siegman, Lasers. University Science Books. Mill Valley. (1986).
88. B. E. Saleh and M. C. Teich, Fundamentals of photonics. john Wiley & sons, (2019).
89. W. T. Silfvast, Laser fundamentals. Cambridge University Press. 2nd edition. (2004).
90. A. E. Siegman, “How to (maybe) measure laser beam quality,” OSA Trends in optics and photonics. (1998).
91. A. H. Firester, M. E. Heller, and P. Sheng, “Knife-edge scanning measurements of subwavelength focused light beams,” Appl Opt. 16(7), 1971–1974 (1977).
92. J. M. Khosrofian, and B. A. Garetz, “Measurement of a Gaussian laser beam diameter through the direct inversion of knife-edge data,” Appl Opt. 22(21), 3406–3410 (1983).
93. M. A.C. de Araújo, R. Silva, E. de Lima, D. P. Pereira, and P. C. de Oliveira, “Measurement of Gaussian laser beam radius using the knife-edge technique: improvement on data analysis,” Appl Opt. 48(2), 393–396 (2009).
94. G. Brost, P. D. Horn, and A. Abtahi, “Convenient spatial profiling of pulsed laser beams,” Appl Opt. 24(1) 38–40 (1985).
95. Y. Suzaki and A. Tachibana, “Measurement of the μm sized radius of Gaussian laser beam using the scanning knife-edge,” Appl. Opt. 14, 2809–2810 (1975).
96. M. B. Schneider and W. W. Webb, “Measurement of submicron laser beam radii,” Appl. Opt. 20, 1382–1388 (1981).
97. J. M. Khosrofian and B. A. Garetz, “Measurement of a Gaussian laser beam diameter through the direct inversion of knife-edge data,” Appl.Opt. 22, 3406–3410 (1983).
98. M. M. Rashad, “Measurements of Laser Beam Using Knife Edge Technique,” Politecnico Milano. Matricola. 883668 18– 19 (2013).
99. K. Fedus, “Development of methods for measuring optical nonlinearities of third order,” Optics [physics.optics]. Université d’Angers, (2011).
100. E. W. V. Stryland and M. Sheik-Bahae, “Z-scan technique for nonlinear materials characterization,” Optical Science, Engineering and Instrumentation. 10291, 97 (1997).
101. J. A. Hermann, “Self-focusing effects and applications using thin nonlinear media,” Journal of Nonlinear Optical Physics & Materials. 1(3), 541–561 (1992).
102. B. Monoszlai, P. S. Nugraha, Gy. Tóth, Gy. Polónyi, L. Pálfalvi, L. Nasi, Z. Ollmann, E. J. Rohwer, G. Gäumann, J. Hebling, T. Feurer, and J. A. Fülöp, “Measurement of four-photon absorption in GaP and ZnTe semiconductors,” Optics Express 28(8), 12352–12362 (2020).
103. Ch. Baumer, C. David, A. Tunyagi, K. Betzler, H. Hesse, E. Kratzig, and M. Wohleckea, “Composition dependence of the ultraviolet absorption edge in lithium tantalate,”Journal of Applied Physics. 93(5), 3102–3104 (2003).
104. M. Yin, H. Li, S. Tang, and W. Ji, “Determination of nonlinear absorption and refraction by single Z-scan method,” Appl. Phys. B. 70, 587–591 (2000).
105. L. Pálfalvi, J. Hebling, G. Almási, Á. Péter, K. Polgár, K. Lengyel, and R. Szipöcs, “Nonlinear refraction and absorption of Mg doped stoichiometric and congruent LiNbO3,” J. Appl. Phys. 95, 902-908 (2004).
106. A. Gaur, H. Syed, B. Yendeti, and V. Rao Soma, “Experimental evidence of two-photon absorption and its saturation in malachite green oxalate: a femtosecond Z-scan study,” JOSA B. 35(11), 2906–2914 (2018).

107. L. Pálfalvi, J. Hebling, J. Kuhl, Á. Péter, K. Polgár, “Temperature dependence of the absorption and refraction of Mg-doped congruent and stoichiometric LiNbO3 in the THz range,” J. Appl. Phys 97(12), 123505 (2005).
108. F. Z. Henari, K. Cazzini, F. ElAkkari, and W. J. Blau, “Beam waist changes in lithium niobate during Zscan measurement,” J. Appl. Phys 78(2), 1373–1375 (1995).
109. F. Freytag, G. Corradi, and M. Imlau, “Atomic insight to lattice distortions caused by carrier self-trapping inoxide materials,” Sci. Rep. 6(1), 36929 (2016).
110. B. Sohn, M. Kang, J. W. Choi, A. M. Agarwal, K. Richardson, and D. T. H. Tan, “Observation of very high order multi-photon absorption in GeSbS chalcogenide glass,” APL Photon. 4(3), 036102 (2019).
111. D. F. Nelson, R.M. Mikulyak, “Refractive indices of congruently melting lithium niobate,” J. Appl. Phys. 45(8), 3688–3689 (1974).
112. O. Gayer, Z. Sacks, E. Galun and A. Arie, “Temperature and wavelength dependent refractive index equations for MgO- doped congruent and stoichiometric LiNbO3,” Appl. Phys. B 91(2),343–348 (2008).
113. G. D. Boyd, R.C. Miller, K. Nassau, W.L. Bond, A. Savage, “LiNbO3: an efficient phase matchable nonlinear optical material,” Appl. Phys. Lett. 5(11), 234–236 (1964).
114. M. Nakamura, S. Higuchi, S. Takekawa, K.Terabe, Y. Furukawa, and K. Kitamura, “Optical Damage Resistance and Refractive Indices in Near-Stoichiometric MgO-Doped LiNbO3,” Jpn. J. Appl. Phys. 41(1), 49–51 (2002).
115. I. Benabdelghani, G.Tóth, G. Krizsán, G. Bazsó, Z. Szaller, N. Mbithi, P. Rácz, P. Dombi, G. Polónyi, and János Hebling, “Three-photon and four-photon absorption in lithium niobate measured by the Z-scan technique,” Opt. Expr. 32(5), 7030–7043 (2024).
116. I. Dolev, A. Ganany-Padowicz, O. Gayer, A. Arie, J. Mangin, G. Gadret, “Linear and nonlinear optical properties of MgO:LiTaO3,” Appl Phys B. 96, 423–432 (2009).
117. I. Shoji, D. Gunji, M. Hakamata, T. Fukui, and Y.Furukawa, “Refractive Indices in Undoped and MgO-Doped Near-Stoichiometric LiTaO3 Crystals,” CLEO/Europe and EQEC, P18 (2011).
118. B. S. Wherrett, “Scaling rules for multiphoton interband absorption in semiconductors,” JOSA B. 1(1), 67–72 (1984).
119. L. A. Lompre, G. Mainfray, C. Manus, J. Thebault, Gy. Farkas, Z. Horvath, “A new effect in multiphoton photo effect of a gold surface induced by picosecond laser pulses,” Appl. Phys. Lett. 33(2), 124–126 (1978).
120. E. W. Van Stryland, M. Sheik-Bahae, A. A. Said, D. J. Hagan, and M. J. Soileau, “Characterization of nonlinear optical materials,” Proc. SPIE. 2114, 444–468 (1994).
121. I. Benabdelghani, G. Bazsó, G.Tóth, P. Rácz, P. Dombi, János Hebling, and G. Polónyi, “Three-photon absorption in lithium tantalate measured by the Z-scan technique”, Optical materials. Submitted, (2024).

Funding

This work was supported and funded by National Research, Development, and Innovation Office (2018-1.2.1-NKP-2018-00009 and 2018 1.2.1-NKP-2018-00010), the Hungarian Scientific Research Fund (OTKA) (12934).